Neutral Hydrogen and Star Formation in the Irregular Galaxy NGC 2366

Deidre A. Hunter Lowell Observatory, 1400 West Mars Hill Road, Flagstaff, Arizona 86001 USA; dah@lowell.edu

Bruce G. Elmegreen

IBM T. J. Watson Research Center, PO Box 218, Yorktown Heights, New York 10598 USA; bge@watson.ibm.com

and

Hugo van Woerden Kapteyn Astronomical Institute, Postbus 800, 9700 AV Groningen, The Netherlands; hugo@astro.rug.nl

ABSTRACT

We present deep UBVJHKH α images and HI maps of the irregular galaxy NGC 2366. Optically, NGC 2366 is a boxy-shaped exponential disk seen at high inclination angle. The scale length and central surface brightness of the disk are normal for late-type galaxies. Although NGC 2366 has been classified as a barred Im galaxy, we do not see any unambiguous observational signature of a bar. There is an asymmetrical extension of stars along one end of the major axis of the galaxy, and this is where the furthest star-forming regions are found, at a radius of 1.3 times the Holmberg radius. The star formation activity of the galaxy is dominated by the supergiant H II complex NGC 2363, but the global star formation rate for NGC 2366 is only moderately elevated relative to other Im galaxies. The star formation activity drops off with radius approximately as the starlight in the inner part of the galaxy but it drops faster in the outer part.

There are some peculiar features of the HI distribution and kinematics. First, the integrated HI shows two ridges running parallel to the major axis that when deprojected appear as a large ring. Second, the velocity field exhibits several large-scale anomalies superposed on a rotating disk; some of these may be from a weak bar that has no Inner Lindblad Resonance. Third, the inclination and position angles derived from the kinematics differ from those derived from the optical and HI morphology. Fourth, there are regions in the HI of unusually high velocity dispersion, but these regions are not associated with the optical galaxy nor any obvious HI feature. Instead the velocity dispersion correlates with a deficit of HI emission in a manner suggestive of long-range, turbulent pressure equilibrium. In other respects the HI is fairly normal. The azimuthally-averaged surface density of HI is comparable to that of other irregulars

in the inner part of the galaxy but drops off slower and extends further in the outer parts. The HI around the star-forming complex NGC 2363 is fairly unremarkable.

Like in other disk galaxies, the gas in NGC 2366 is lumpy and star-forming regions are associated with these HI complexes. H II regions are found where the gas densities locally exceed 6 M_{\odot} pc⁻². This threshold is required to provide a cool phase of HI as a first step toward star formation. NGC 2366, like other irregulars, has low gas densities relative to the critical gas densities of gravitational instability models, so large-scale gravitational instabilities operate slowly or not at all. Considering the lack of shear in the optical part of this galaxy, the relative slowness of such instabilities may not be a problem – there is little competition to the slow gravitational contraction that follows energy dissipation. This differs from the situation in giant spiral disks where the shear time is short, comparable to the energy dissipation time, and strong self-gravity is required for a condensation to grow and dissipate its turbulent energy before it shears away.

The sub-threshold surface densities are also not unusual if they are viewed using the critical tidal density for gravitational self-binding of a rotating cloud, rather than the critical surface density from the usual disk instability condition. The peak densities in all regions of star formation are equal to the local tidal densities, giving an agreement between these two quantities that is much better than between the surface density and the critical value. Evidently the large scale gas concentrations are all marginally bound against background galactic tidal forces. This condition for self-binding may be more fundamental than the instability condition because it is local, three-dimensional, and does not involve spiral arm generation as an intermediate step toward star formation.

Subject headings: galaxies: irregular — galaxies: star formation — galaxies: individual: NGC 2366 — galaxies: ISM — galaxies: kinematics and dynamics

1. Introduction

NGC 2366 is classed as a barred Magellanic-type irregular (IBm) galaxy (de Vaucouleurs et al. 1991). The distance of 3.44 Mpc that we adopt here, determined by Tolstoy et al. (1995) from cepheid light curves, places NGC 2366 in the M81 Group of galaxies (Karachentseva, Karachentsev, & Börngen 1985). The nearest galaxy is the Scd NGC 2403 at 290 kpc. NGC 2366 has an M_B of -16.5 which is close to that of the Small Magellanic Cloud, and in terms of color, luminosity, and size NGC 2366 is a typical irregular galaxy (Hunter 1997). However, NGC 2366 is unusual in that it contains the supergiant H II complex NGC 2363 at the southwest end of the galaxy (Youngblood & Hunter 1999). NGC 2363 has the same brightness in $H\alpha$, corrected for extinction, as the prototype supergiant H II complex, the 30 Doradus nebula in the Large Magellanic Cloud, and contains a large fraction of the total current star-formation activity of the

galaxy (Aparicio et al. 1995, Drissen et al. 2000). However, there is also another very large H_{II} complex to the west of NGC 2363 as well as numerous smaller H_{II} regions scattered along the disk. Because of the presence of these two very large H_{II} complexes, NGC 2366 has an inferred star formation rate that is towards the high end of the distribution for normal Im galaxies.

In this paper we present optical, near-infrared, and HI radio interferometer images of NGC 2366 for a comprehensive view of the galaxy. We analyze them to learn about the star formation processes in this galaxy.

2. The Observations

2.1. The HI

We obtained 21 cm line-emission observations of NGC 2366 with the Very Large Array (VLA¹) radio interferometer in its C and D-array configurations. The C-array observations were made 1989 July 21 with a total on-source time of 235 minutes. The D-array observations were made 1989 November 7 with a total on-source time of 331 minutes. The total bandwidth was 3.125 MHz with a channel separation of 24.414 kHz, that equals 5.16 km s⁻¹. However, a total of only 64 channels was allowed at that time because of computer limitations, and so the velocity coverage is only 330 km s⁻¹. The data were on-line Hanning-smoothed, and the resulting velocity resolution is 10 km s⁻¹. The central heliocentric velocity was 107 km s⁻¹. The field center is 7^h 23^m 34.2^s, +69° 18′ 42″ (equinox 1950, here and throughout).

We subtracted the continuum emission in the uv-plane using line-free channels on either end of the spectrum and combined the data from the different arrays. To make maps, we employed a routine in NRAO's Astronomical Image Processing System (AIPS) that enables one to choose a sample weighting that is in between the standard "natural" weighting, which gives the highest signal-to-noise but at the expense of long wings in the beam, and "uniform" weighting, which gives the best resolution but at the cost of signal-to-noise and the presence of negative sidelobes. We chose a sample weighting that gives a formal increase of only 5% in noise yet with a significant improvement in beam profile over what would have been achieved with "natural" weighting. The resulting synthesized beam profile (FWHM) is $33.6'' \times 28.9''$. This corresponds to 560 pc×480 pc at the galaxy. We deconvolved the maps until there were roughly comparable numbers of positive and negative components. The rms noise in the cleaned channel maps is 1.09 mJy beam⁻¹. We also constructed a map cube from the C-array data by itself in order to take advantage of that array's higher resolution. The resulting synthesized beam profile of those maps is $17.8'' \times 13.2''$ (300 pc×220 pc at the galaxy), and the rms noise in a cleaned channel map is 1.9 mJy beam⁻¹. (Channel maps of the C+D-array HI data cube are discussed in Section §5).

¹ The VLA is a facility of the National Radio Astronomy Observatory (NRAO), itself a facility of the National Science Foundation that is operated by Associated Universities, Inc.

To remove the portions of each channel map without emission that are only contributing noise to the map, we used the maps smoothed to twice the beamsize for a conditional transfer of data in the unsmoothed maps. The channel maps were blanked wherever the flux in the smoothed maps fell below 2.5σ . Flux-weighted moment maps were made from the resulting data cube.

The flux in each channel of the C+D-array data cube was integrated over a square 30' on a side, corresponding approximately to the diameter of the primary beam of the telescope, in order to determine the total HI flux detected in the maps. The fluxes were corrected for attenuation by the primary beam. To compare with a single-dish observation we integrated the flux over a square 10' on a side as well. These integrated profiles are shown and compared to the single-dish observation of Hunter, Gallagher, & Rautenkranz (1982) in Figure 1. Our integrated flux from the 10' box has a peak that is 12% higher than the peak from the single-dish telescope with a 10' beam. The total integrated flux profile (over 30') is about 36% higher than the single-dish profile. Therefore, we recover all of the gas observed in the 10' single-dish observation as well as more gas extended beyond that.

The total HI mass detected within the primary beam of the VLA observations is 8.0×10^8 ${\rm M}_{\odot}$. This is smaller by a factor of 10 than what was measured by Thuan & Martin (1981) using the NRAO 91 m telescope (10' beam); only a few percent different from the mass reported by Huchtmeier, Seiradakis, & Materne (1981) from single-dish mapping; 1.5 times larger than what is reported by Wevers, van der Kruit, & Allen (1986) from single-dish mapping; and 10% larger than the mass given by Swaters (1999) from single-dish mapping. Thus, our integrated HI mass is close to values determined by others; the Thuan and Martin value appears to be mistaken.

2.2. Optical Images

Deep UBV images were kindly obtained for us by P. Massey using a Tektronix 2048×2048 CCD on the Kitt Peak National Observatory 4 m telescope 1998 January. The telescope position was offset 30" between the three images taken in each filter in order to improve the final flat-fielding. Exposure times of 1800 s, 480 s, and 180 s for UBV, respectively, were used. The electronic pedestal was subtracted using the overscan strip, and the images were flat-fielded using dome and sky flats. Landolt (1992) standard stars were used to calibrate the photometry. The pixel scale was 0.42", the seeing was ~ 1.6 ".

Deep H α images of NGC 2366 were obtained using the Perkins 1.8 m telescope at Lowell Observatory during 3 observing runs 1994 to 1995. The observations used an 800×800 TI CCD provided to Lowell Observatory by the National Science Foundation, the Ohio State University Fabry-Perot that was used simply as a 3:1 focal reducer, an H α filter with a FWHM of 32 Angstroms, and an off-band filter centered at 6440 Angstroms with a FWHM of 95 Angstroms. The off-band filter was used to subtract stellar continuum from the H α filter to leave only H α nebular emission. In order to survey the entire galaxy, 6 separate pointings were mosaicked

to produce the final H α image. Observations consisted of several 1800 s or 3000 s images per pointing. The pixel scale was 0.49", and the seeing was ~ 2.3 ".

2.3. Near-Infrared Images

Near-infrared JHK images of NGC 2366 were obtained using the Ohio State Infrared Imager-Spectrograph on the Perkins 1.8 m telescope in two observing runs in 1996 and 1997. The pixel scale was 1.5", the field of view was 6.4', and the effective seeing was 3". Observations alternated between the galaxy and a separate sky position every 1–2 minutes. Upon each return to the galaxy, the position was offset by 10" around the chip so that the numerous bad pixels would not appear in the same place each time and to aid in removal of stars in the sky frame. A correction for deviation from linearity with increasing signal level was applied to each of the 4 detectors, observations of a dark filter were subtracted, and flat-field frames were used to remove pixel-to-pixel variations. The flat-field was determined by observations of a white screen in the dome, and images made with the illuminating lamp off were subtracted from the images taken with the lamp on. Sky-subtracted images were aligned and combined. The "UKIRT" standard stars from the list compiled by S. Courteau were used to calibrate the photometry, and so the photometry is on the UKIRT system. The California Institute of Technology (CIT) photometric system is 8% bluer in J-H and 4% bluer in H-K compared to the UKIRT system.

A check on our photometry is provided by comparison to aperture photometry done by others. Aaronson, Mould, & Huchra (1980) measured an H magnitude of 10.44±0.08 for NGC 2366 through a 165.2" diameter aperture. We measure an H magnitude that is 0.37 magnitudes fainter. Their measurement through an aperture of 110.6" diameter is also brighter. On the other hand, our H-band measurement integrated to a radius of 117.5" differs by only 0.01 magnitude from that given by Pierini et al. (1997).

3. Radio Continuum

To examine continuum objects in the field of view of the radio maps, we constructed and deconvolved maps from the C+D-array uv-data before the continuum was subtracted. We summed channels not containing HI emission from NGC 2366. The 21 cm continuum emission within the primary beam of the VLA is shown in Figure 2, and the fluxes of all of the sources in the field of view of the primary beam are given in Table 1. Only source 7 lies within the field of view of our V-band image, and we do not detect any corresponding optical object there.

In Figure 3 we show contours of the continuum emission superposed on the H α image of the galaxy, In NGC 2366, we have primarily detected the supergiant H II region NGC 2363 although there is some continuum emission in the direction of the giant H II region to the west of NGC 2363 and some emission extending to the north of NGC 2363. Radio continuum observations of NGC

2363 at other wavelengths have shown the emission to be that of an optically thin, ionized gas (Klein & Gräve 1986), as expected.

4. The Optical and Near-Infrared View of the Galaxy

4.1. General Morphology

Our V-band image of NGC 2366 is shown in Figures 4 and 5. In the deep display (Figure 4) one can see that NGC 2366 is elliptical-shaped with a high degree of ellipticity implying a relatively high inclination angle. Although the bulk of the galaxy is contained within regular isophotes, there is an extension of starlight at a faint surface brightness level along the major axis to the southwest. This extension is highlighted by a superposed contour at 26.54 magnitudes arcsec⁻² in Figure 4. This low surface brightness starlight is not mirrored at the northeast end of the major axis. The shallower display of the V-band image (Figure 5) shows an inner cigar-shaped morphology dominated by the giant star-forming region NGC 2363 at the southwest end of the galaxy. An intermediate surface brightness contour in Figure 5 (the second faintest one) illustrates an additional asymmetry of starlight within the galaxy that skews the contour to the northwest in the northeastern part of the galaxy and to the southeast in the southwestern part of the galaxy. This skewing could be described as an asymmetrical warp, but it is not found in the outer contours.

4.2. Bar Structures

NGC 2366 is classified as a barred Im galaxy and the cigar-shaped morphology contributes to the impression that the galaxy is barred. However, identifying bar structures in irregular galaxies is difficult from morphology alone. As discussed by Roye & Hunter (2000), this identification is complicated by the lack of symmetry provided by spiral arms coming out of the nucleus or bar. It is particularly complicated in galaxies that are also inclined and often boxy in shape. This is especially difficult if the bar is comparable in size to the entire galaxy as appears to be the case in, for example, NGC 4449 (Hunter, van Woerden, & Gallagher 1999). Does NGC 2366 contain an over-sized bar structure, or does it just appear bar-like because it is highly inclined?

We have explored the possible presence of bars in NGC 2366 by fitting elliptical structures to isophotes. According to Athanassoula et al. (1990), a bar can be fit with a curve of the form $(\frac{|x|}{a})^c + (\frac{|y|}{b})^c = 1$, where a and b are the semi-major and minor axes and c is a parameter that describes the boxiness of the bar structure. For c = 2 the structure is an ellipse, for c < 2 the structure is "disky," and for c > 2 the structure is "boxy." In NGC 2366, we have fit the inner and outer parts well with a curve with c = 3.0, indicating a boxy shape.

First, we fit the outer isophote at 25.66 magnitudes arcsec⁻² (seen as the inner of the two

isophotes in Figure 4) with a curve that is shown superposed on the V-band image in Figure 4 as a thick smooth contour. The isophotes in Figure 4 are determined from a smoothed version of the V-band image to improve signal-to-noise in the outer parts. One can see that, if we exclude the faint extension to the southwest encompassed by the fainter isophote at 26.54 magnitudes $arcsec^{-2}$, the contour at 25.66 magnitudes $arcsec^{-2}$ nicely encompasses the bulk of the optical galaxy. This outer "bar" has a semi-major axis of $1.6R_{25}$ at a position angle of 32.5° , where R_{25} is the radius of the galaxy at a surface brightness of 25 magnitude $arcsec^{-2}$ in B. The minor-to-major axis ratio b/a is 0.42. If the b/a ratio reflects the inclination of the galaxy and the intrinsic ratio of the disk is taken to be 0.3 (Hodge & Hitchcock 1966, van den Bergh 1988), the inclination shown by the outer galaxy is 72° .

Second, we fit bar structures to two inner isophotes that are more normal in size compared to bars in spirals. These are shown as thick contours in the inner part of Figure 5. The thick outer contour is reproduced from Figure 4. One of the inner fits excludes the supergiant H II region NGC 2363 and the other includes it since it has been argued that the formation of NGC 2363 may have been facilitated by placement at the end of a bar (Elmegreen & Elmegreen 1980). The sizes, position angles, b/a, and centers of these two bar fits, as well as characteristics of the fit to the outer galaxy, are listed in Table 2. One can see that all three fits have nearly the same position angle. We are not seeing a twisting of the isophotes from the inner to the outer galaxy which in spiral galaxies is a good clue to the presence of a bar. The center of the middle isophote is offset from the center of the outer isophote 19" east and 8" north. The center of the inner isophote is offset 33" east and 31" north because the inner one does not include NGC 2363.

Figure 5 also shows the observed isophotes at 26.54, 25.66, 24.04, 23.04, and 22.68 magnitudes arcsec⁻². The contour at 24.04 mag arcsec⁻² illustrates the skewing of the V-band image that was discussed above. We will return to this skewed contour in section 5.5 below.

In addition to these three carefully selected isophotes that we fit with ellipses by hand, we have done automatic elliptical isophote fitting of the entire V-band image of the galaxy. We used annuli of 63'' width out to a radius of 7.4', and allowed the fitting procedure to fit position, ellipticity, and position angle for each ellipse. This routine does not allow the boxy structures that we used above—only ellipses. The results of this type of general fitting procedure should be viewed with caution in lumpy galaxies like NGC 2366, where young regions here and there can highly influence the fitting. We found that the inclination angle varied from 68° to 79° and the position angle varied from 29° to 34° . Most of the variation—a decrease outward in position angle and inclination—occurred in the inner 3' of the galaxy. Some of this variation is undoubtedly due to the difficulty in fitting just mentioned, but it is also possible that some of the variation is the signature of a bar structure with a semi-major axis of $\sim 3'$.

If the outer isophote is a true bar, its b/a ratio of 0.42 falls within the range of what is observed for bars in late-type spirals (Martin 1995). However, a/R_{25} is 1.6 in NGC 2366. In spirals the ratio a/R_{25} is much smaller: 0.2 for Sd–Sm galaxies (Elmegreen et al. 1996), 0.05–0.25

for Sd–Sdm spirals (Martin 1995), and 0.25–0.3 for Sd's with exponential bars (Elmegreen & Elmegreen 1985). The bar fit to the inner isophote would be reasonable in size compared to these values, while the middle isophote fit would still be a bit large by comparison.

Surface brightness cuts, 33" wide, along the major and minor axis of the inner bar are shown in Figure 6. Neither cut can be reasonably fit with a Gaussian profile, as they are in a sample of early-type spirals observed by Ohta, Hamabe, & Wakamatsu (1990). The shapes of the minor and major axis cuts individually resemble a few of those observed in late-type barred spirals by Elmegreen et al. (1996). Among barred late-type spirals (Combes & Elmegreen 1993, Elmegreen et al. 1996) the bar is commonly well-fit with an exponential whereas in early-type spirals the bars tend to be more uniform in intensity.

Thus, we find three isophotes that could be claimed to be bar structures: an inner one that places the supergiant H II region NGC 2363 at one end, a middle structure that includes NGC 2363, and an outer structure that encompasses most of the galaxy. From the surface photometry there is no compelling evidence that any of these structures is a true bar, but we will return to this issue below when we present the HI data and the velocity field of the gas.

4.3. Surface Photometry

UBVJHK surface photometry is shown in Figures 7 and 8 (see also Wevers et al. 1986). We used ellipses with a position angle of 32.5°, ellipticity corresponding to an inclination of 72°, and a semi-major axis step size of 21". The inclination, position angle, and center were determined from the outer isophote shown in Figure 4. The surface photometry and colors have been corrected for reddening using a total $E(B-V)_t=E(B-V)_f+0.05$, where the foreground reddening $E(B-V)_f$ is 0.043 (Burstein & Heiles 1984). We use the reddening law of Cardelli, Clayton, & Mathis (1989) and $A_V/E(B-V)=3.1$. Thus, A_V is 0.29 and E(U-B) is 0.06.

We determined R_{25} to be 2.6' (=2.6 kpc). Our radius is 27% bigger than that given by de Vaucouleurs et al. (1991). The Holmberg radius, R_H , originally defined to a photographic surface brightness, is measured at an equivalent B-band surface brightness $\mu_B = 26.7 - 0.149(B - V)$. For a $(B-V)_0$ of 0.27, the Holmberg radius is determined at a μ_B^0 of 26.66 magnitudes arcsec⁻². We find that R_H is 5.1' (=5.1 kpc). Both R_{25} and R_H are determined from the reddening corrected surface photometry. Global properties of NGC 2366 are listed in Table 3.

We fit an exponential disk to μ_V^0 , excluding the central 1.2', and the fit is shown in Figure 7. Except for the central region, NGC 2366 is fit well with an exponential disk profile having a central surface brightness μ_0 of 22.82±0.09 magnitudes $arcsec^{-2}$ and a disk scale length R_D of 1.59±0.04 kpc. This same exponential also fits μ_J reasonably well over the radii where the J-band is detected. Noeske et al. (2000) have found a scale length of half this— 0.88±0.03 kpc and 0.82±0.03 kpc for B and I-bands, respectively— from fitting the inner 2.7' of the galaxy. De Jong (1996) has determined disk characteristics of a large sample of galaxies spanning a wide range in

type. NGC 2366 has a central surface brightness, corrected to the B passband, and an R_D that are in the middle of the range of what de Jong finds for late-type galaxies.

The integrated colors of NGC 2366 are similar to those of the luminous irregular NGC 4449 with the exception that NGC 2366 is 0.1–0.2 magnitude bluer in the near-infrared (Hunter et al. 1999). Like in most irregulars, colors in NGC 2366 are fairly constant with radius (see also Wevers 1984). Integrated values are given in Table 3, and annular colors are shown in Figures 7 and 8.

These figures indicate that NGC 2366 does not exhibit any major color gradient with radius. It is common lore that irregular galaxies do not have color gradients, and NGC 2366 appears to be perfectly consistent with that, now frequent, assumption. However, in the case of NGC 2366, and by extension other irregulars, azimuthally-averaged colors do not in fact tell the whole story. In Figure 9 we show a B/V ratio image, averaged 3×3 pixels to improve the signal-to-noise. Although the galaxy is relatively constant in color with radius in an average sense, there are color variations on large scales. (The red circular region in the Figure at $\sim 7^h$ 23^m 30^s, 69° 21' is due to bright foreground stars.) In Figure 9 one can see a long, blue ridge running the extent of the galaxy, including the central bars identified in Figure 5 and the unusual, off-axis higher surface brightness extensions to the northwest and southeast. A 1.5 kpc diameter region $\sim 50''$ to the west/southwest of the center has a redder stellar population. This coincides with the center of the HI ring just to the north of NGC 2363 discussed below. It is 0.1–0.15 mag redder than the bluer areas of the galaxy outside of H II regions. Another large, low surface brightness region $\sim 2.5'$ to the northeast of center also has a red stellar population. The western part of NGC 2363 also stands out as red, presumably due to the dust that obscures the massive star cluster there (Drissen et al. 2000). The faint southwest extension of stars outlined by the outer isophote in Figure 4 has colors like those of most of the rest of the background galaxy that does not contain HII regions.

4.4. Star-Forming Regions

Our H α image of NGC 2366 is shown in Figure 3, and the central portion was also shown by Hunter, Hawley, & Gallagher (1993) in their study of the extra-H II region ionized gas. Although there are numerous star-forming regions in NGC 2366, the H α morphology is dominated by two very large H II complexes: NGC 2363 (numbered I and II by Drissen et al. 2000) and a second one directly to the west of NGC 2363 (numbered III by Drissen et al. 2000). Supergiant H II regions like these are rare among normal irregular galaxies (Youngblood & Hunter 1999).

NGC 2363 has an $L_{H\alpha,0}$ of 1.3×10^{40} ergs s⁻¹. This represents 70% of the galaxy's total $H\alpha$ luminosity. NGC 2363 has the $H\alpha$ equivalent of the 30 Doradus nebula, where 30 Doradus is the supergiant H II region in the Large Magellanic Cloud that is often taken as defining the class of supergiant H II complexes. (The extinction corrected $H\alpha$ luminosity of 30 Doradus is taken as 1.5×10^{40} erg s⁻¹, from Kennicutt 1984). The $H\alpha$ luminosity is what would be expected of 1260 O7V stars.

Figure 3 does not include two tiny H II regions that are located south of NGC 2363 by 2.7′ and 3.0′. (They can be seen in Figure 14 near 7^h 23^m , 69° 14′). They are in fact the furthest H II regions from the center of the galaxy and are located at 6.6 kpc and 5.9 kpc radius in the plane of the galaxy. The furthest H II region corresponds to a distance of $2.5R_{25}$ or $1.3R_H$. They are part of the faint extension of starlight along the major axis to the southwest seen in the V-band in Figure 4.

In Figure 10 we show the azimuthally-averaged H α surface brightness and compare it to μ_V^0 . Once past the H II region NGC 2363, the H α surface brightness first drops off at a rate roughly comparable to the starlight, but then beyond 4.5 kpc drops off faster. The current star formation activity ends before the detected starlight ends. The outer 16% of the galaxy by area in which we detect starlight contains no detectable H II region.

The H α luminosity and derived star formation rates of the galaxy are given in Table 3. NGC 2366 has a star formation rate per unit area that is normal, but towards the high end of the range, for irregular galaxies (Hunter 1997). At its current rate of consumption, the galaxy can turn gas into stars for another 8 Gyr if all of the gas associated with the galaxy can be used. The timescale to run out of gas becomes 12–32 Gyr if recycling of gas from dying stars is also considered (Kennicutt, Tamblyn, & Congdon 1994). These timescales to exhaust the gas are somewhat short for irregular galaxies (Hunter 1997), but, nevertheless, the galaxy is in no danger of running out of the fuel for star formation any time soon.

5. The HI

NGC 2366 was first mapped in HI with the single-dish radio telescope at Effelsberg (Huchtmeier et al. 1981). They reported that the HI covers 30'. Wevers et al. (1986) presented Westerbork observations with a 25" beam and 16.5 km s⁻¹ channel separation, and recently, Swaters (1999) has presented new Westerbork observations with a 30" beam and 2–4 km s⁻¹ channel separation. Braun (1995) discussed 9" resolution VLA B+C+D-array observations with 5.16 km s⁻¹ channel separation. Our VLA C+D-array observations, with much longer integration times than Braun's data, contribute medium spatial resolution observations with fairly high velocity resolution at high sensitivity.

Channel maps of the C+D-array HI data cube are presented in Figure 11. We detect HI emission from 24.5 km s^{-1} to 174.0 km s^{-1} , and one can see general rotation from the northeast, at higher radial velocities, to the southwest, at lower radial velocities. There is also some interesting low column density emission that appears in the northeast part of the galaxy at velocities $102-138 \text{ km s}^{-1}$. There may be a weak counterpart to the south, at velocities $61-81 \text{ km s}^{-1}$. One ridge of HI is clearly seen at velocities of $61-117 \text{ km s}^{-1}$, and a second ridge at $117-153 \text{ km s}^{-1}$.

The integrated HI is shown in Figure 12—two displays to show both the fainter emission in the outer parts and the inner, higher column density material near the center. To help the

reader orient the HI with respect to the optical galaxy, Figure 12 shows one of the contours from the V-band image (Figure 4). We detect HI emission to a radius of 11.7' at a column density of 1.7×10^{19} cm⁻². Huchtmeier et al. (1981) reported that the HI in NGC 2366 is extended to a radius of 15' at 10^{19} atoms cm⁻². However, in view of the smearing introduced by the Effelsberg beam (FWHM \sim 8.8'), the results could be consistent. VLA maps of the extended HI around NGC 2366 are under analysis and will settle this issue.

In the integrated HI map, one can see large clumps of gas within the optical galaxy, arranged approximately in two parallel ridges of HI. Deprojected, the HI appears as a ring with a depression in the middle, similar to Sextans A (Skillman et al. 1988). The ring has a diameter of 5.5 kpc. Two-dimensional ratio images of the B and V-bands suggest that the center of this ring is redder than the surrounding stellar populations (Figure 9). The center of the ring $(7^h \ 23^m \ 31.3^s, 69^\circ \ 19' \ 53'')$ is to the north of the kinematical center and the center of the outer optical isophote by a little more than 1'.

The ridges of gas are surrounded by a more extended relatively smooth distribution of gas. However, in the outer parts we do see a cloud in the southwest surrounded by more diffuse emission. In the northeast we see a somewhat unusual extension that looks like a "knob" extending east from the galaxy with some filamentary material extending south of it. There is also some filamentary HI emission to the north of the galaxy center around 7^h 23^m 45^s , 69° 24'.

One can also see that the outer shape of the HI distribution is generally consistent with that of the optical galaxy. Specifically, the morphology of the integrated HI indicates a position angle of 23.5° and b/a of 0.41. This position angle is 9° smaller (HI oriented further towards the north) than what we see for the optical galaxy, but the minor-to-major axis ratio is the same. However, the HI is not centered symmetrically on the optical galaxy. The HI extends further to the northeast than to the southwest relative to the V-band isophote: The center of the HI morphology is shifted 47'' to the east and 54'' to the north from the center of the outer optical isophotes. However, asymmetric distributions of HI are common among disk galaxies (Richter & Sancisi 1994).

5.1. Surface Density

In Figure 13 we show the azimuthally-averaged surface density of the HI gas in NGC 2366. We have integrated the HI in 25" radial steps. In determining the surface density, we had to choose a position angle and inclination which is somewhat problematical given the selection available in Table 2, particularly including the different values we will find below from the kinematics of the HI. In this plot we show the surface density that results from two choices of position angle and inclination: 1) the values that result from the HI morphology (23° position angle and 73° inclination) and 2) the values that result from the kinematics of the HI (46° position angle and 65° inclination). The choice of the kinematic parameters implies that the HI distribution is not

circularly symmetric but elongated. The choice of the morphologically-derived parameters implies that the HI distribution is axisymmetric, but that there are non-circular motions. We present both cases, but the conclusions are the same for either choice of parameters.

From the Figure we see that, outside the center (>1.75'), the gas surface density drops off fairly smoothly. In order to compare the surface brightnesses in HI, H α , and V-band, we have plotted the logarithm of Σ_{HI} , the logarithm of $\Sigma_{H\alpha,0}$, and μ_V^0 in magnitudes over the same logarithmic interval. These are shown in the right panel of Figure 13. There we can see that the HI surface density drops off much more slowly than the starlight or star formation activity. This is also what we found for the IBm galaxy NGC 4449 (Hunter et al. 1999).

In the left panel of Figure 13 we compare the gas surface density profile of NGC 2366 to that of average Im, Sdm, and Sd galaxies. The average profile for Im galaxies comes from Broeils & van Woerden (1994) and those for the spirals from Cayatte et al. (1994) who obtained the data for individual galaxies from Broeils and van Woerden and Warmels (1988). This type of comparison requires that the observations be at similar physical spatial resolutions and that there be many resolution elements across the galaxy. The beam of our NGC 2366 observations is small compared to the HI extent of the galaxy which is about 21 beam-widths in radius. The observations of Im galaxies by Broeils and van Woerden have HPBWs of 340–1020 pc with a median of 400 pc (for an H_0 of 65 km s⁻¹ Mpc⁻¹). This is comparable to our NGC 2366 resolution of 560 pc×480. The HPBWs of the observations of spirals, on the other hand, vary from 530 pc to 5190 pc (median of 2600 pc for Sdm and 1070 pc for Sd galaxies). Therefore, the profiles for the spirals are affected by a larger beam size compared to that of NGC 2366.

What we see in Figure 13 is that the HI surface density of NGC 2366 is comparable to the average of a sample of Im galaxies in the inner 3.5′. The NGC 2363 complex is dominating at $R/R_{25} \sim 0.7$. Beyond 3.5′ the HI falls off more slowly than in other Im galaxies and the HI extends much further. The spiral samples on average have much lower surface densities in the center, perhaps because of resolution effects and the fact that the gas is dominated by molecular material rather than atomic (Honma, Sofue, & Arimoto 1995), and drop quickly at smaller radii.

5.2. Relationship of HI to Integrated Starlight

In NGC 2366 the ratio of integrated HI content to starlight, M_{HI}/L_B , is 1.36 $M_{\odot}/L_{B,\odot}$. The average M_{HI}/L_B ratio measured by Broeils & Rhee (1997) from their sample of galaxies is $0.36\pm0.47~M_{\odot}/L_{B,\odot}$ for all morphological types and 0.32 for Im galaxies. For a large sample of irregulars Roberts & Haynes (1994; see also Roberts 1969) show a median M_{HI}/L_B of about $0.6~M_{\odot}/L_{B,\odot}$ for Im galaxies. NGC 2366, therefore, appears to be unusually gas rich for its luminosity by a factor of $\sim 2-4$.

Bothun (1984) has suggested that a better ratio to consider is $M_{HI}/L_{H(-0.5)}$ where $L_{H(-0.5)}$ is the luminosity of the galaxy in the H-band within an aperture A of log A/D = -0.5, where D is

the size of the galaxy in the optical. As originally defined, A corresponds to a radius of $0.316R_0$ where R_0 is close to R_{25} . Bothun showed that $M_{HI}/L_{H(-0.5)}$ is a function of the luminosity of the galaxy. For a galaxy like NGC 2366 with a total $M_{B,0}$ of -17, the ratio $M_{HI}/L_{H(-0.5)}$ would be expected to be of order 1.8, and Broeils & Rhee (1997) measured an average $M_{HI}/L_{H(-0.5)}$ of 0.5 ± 0.5 for their sample of galaxies. Instead, we measure the $M_{HI}/L_{H(-0.5)}$ ratio to be 13, which is 7 times higher than expected for this luminosity. In this comparison NGC 2366 is very much more gas-rich than other galaxies for its luminosity. The integrated HI measurements of spirals used by Broeils and Rhee from interferometer data agree within a few percent with single-dish observations (Broeils & van Woerden 1994) and thus it is unlikely that they are missing significant amounts of HI. On the other hand, their Figure 1 shows $M_{HI}/L_{H(-0.5)}$ increasing with Hubble type and they do not include galaxies later than type Sd, for which the average $M_{HI}/L_{H(-0.5)}$ is \sim 1. Thus, it could be that NGC 2366 is not too unusual for its Hubble type, but it is certainly much gassier than Sd-type galaxies. More H-band observations of irregulars are needed to determine how unusual are NGC 2366 and NGC 4449, also with an unusually high $M_{HI}/L_{H(-0.5)}$ (Hunter et al. 1995), for their morphological type.

5.3. Relationship of HI to $H\alpha$

In Figure 14 we show contours of HI superposed on our H α image. We see that, with the exception of the two faint H II regions to the south of NGC 2363, star formation is found within an observed HI column density exceeding 2×10^{21} atoms cm⁻². The two extreme southern H II regions sit within a column density contour of half that. In addition, the H II regions are primarily associated with local peaks in the HI. In particular, most of the H II regions lie along the eastern HI ridge.

In Figure 15 we compare the HI and H α brightnesses of individual pixels in the galaxy, where the H α image has been averaged 15×15 pixels in order to approximately match the HI pixel size in the C+D-array map. The x-axis of this figure goes from zero to an observed HI column density of 5.2×10^{21} atoms cm⁻². The y-axis goes from an H α luminosity of 7.2×10^{33} ergs s⁻¹ to 1.4×10^{37} ergs s⁻¹, corrected for reddening (1 count in the H α image is 1.1×10^{33} ergs s⁻¹; we have not converted this to a surface brightness by dividing by the area of the pixel). H α is corrected for reddening assuming E(B-V)_t=E(B-V)_f+0.1=0.143. With a Cardelli et al. (1989) reddening curve, $A_{H\alpha}$ =0.36. There is a trend that the highest H α luminosities are found at the highest observed HI column densities.

5.4. Velocity Field

The HI velocity field of NGC 2366 is shown in Figure 16. We have fit the velocity field in the following manner. We began by allowing all parameters to be variables and fitting the entire field

with a Brandt function. From the resulting solution we fixed the center coordinates. These are given in Table 2. We then fit the inner 150" radius of the velocity field with solid body rotation and from that fixed the systemic velocity at 99.1 ± 0.2 km s⁻¹. We did this for inclination angles of 56° and 72° and the two resulting systemic velocities agreed to 2 km s⁻¹. (Swaters [1999] reports a systemic velocity of 104 km s⁻¹, and Wevers et al. [1986] report 98 km s⁻¹). We then fit tilted ring models to annuli of 20" width out to a radius of 460", allowing the inclination, position angle, and rotation speed to vary and trying three different initial guesses. We found that the receding side, corresponding to the northeast portion of the galaxy, produced more stable solutions than the approaching or southwest side, and emphasis was placed on the receding side in determining the final solution. In addition the fitting routine was unable to fit the innermost ring. We also found that beyond a radius of 150" the position angle and inclination were approximately constant. The variations of position angle and inclination with radius are shown in Figure 17. The position angle and inclination were determined from the 150" < R < 460" portion of the fit. Finally, we fixed the position angle and inclination and fit the rotation speed again for each annulus using annuli of 20" width to a radius of 460" and annuli of 40" width beyond there to 620". We also used the higher resolution C-array velocity field to examine the kinematics in the inner 3' with 10" rings. The uncertainties were higher but the results were essentially the same as for the C+D-array field.

The final position angle and inclination determined from the HI kinematics are listed with the others determined from the optical and HI morphology in Table 2. We determine an inclination angle of 65° and a position angle of 46°. This can be compared to 58° and 39°, respectively, determined by Braun (1995) from high resolution B-array VLA data; 65° and 40° determined by Wevers et al. (1986); and 59° and 42° determined by Swaters (1999); thus, the agreement is good. However, the inclination and position angles determined from the HI velocity field are not the same as those found from the optical or HI morphologies. The morphologies of the stars and gas both give axis ratios that imply an inclination of about 72°, while the fit to the velocity field suggests that the HI is 7° less inclined. The position angle of the velocity field is also rotated further to the east than the morphology of the stars or gas would suggest by 14–22°. These results indicate that either the HI distribution or the kinematics deviate from axisymmetry. That is, the HI disk must be either elongated or warped or the motions must be non-circular.

The resulting inclination-corrected rotation curve is shown in Figure 17 (adopting the inclination of 65° determined from the fit to the velocity field), and contours of the model rotation curve are superposed on the velocity field in Figure 16. The kinematical center of the gas is shifted 5" to the east and 17" to the north of the center of the outer optical isophotes, but these offsets are less than one beam-width. One can see in Figure 16 (and Figure 18 below) that the velocity field is distorted to the southeast of the center of the galaxy, and this causes problems in fitting the approaching side of the velocity field. This region of the velocity field has no obvious connection with any optical, integrated HI, or velocity dispersion feature. In fact, the anomalous region is outside the V-band contour shown in Figure 16. Furthermore, the distortion in the velocity field is not the S-shape of a warp (Bosma 1981). There is also a distortion to the north of the galaxy

center, and the isovelocity contours on the outer west side of the galaxy generally twist to become oriented north-south at the edge of the HI distribution (see Figures 16 and 18).

In spite of all this the rotation curve shown in Figure 17 is fairly normal. It rises like a solid body for approximately the inner 110'' (=0.7R₂₅), rises less steeply to $\sim 1.1R_{25}$, and then levels off. At a radius of about 340'' (=2.2R₂₅), the rotation curve begins to fall although the approaching and receding sides behave differently, with the approaching side remaining approximately level. The maximum rotation speed is 48 km s⁻¹. Swaters (1999) gives a rotation speed of 60 km s⁻¹ at his last measured radius of 5.9'; the difference is consistent with his lower value for the inclination.

5.5. Bar Structure Revisited

If the galaxy contains a stellar bar potential, we might expect this to be reflected in velocity field anomalies in the vicinity of the bar—in the isovelocity contours or changes in position angle or inclination (for example, Pisano, Wilcots, & Elmegreen 1998; Koribalski et al. 1996; Ondrechen & van der Hulst 1989). In the velocity field (Figures 16 and 18) there is a hint of a position angle greater than 45° for radii less than 1.5′. This could, if real, be a bar effect. However, clear and obvious changes in the position angle or inclination with radius that could correspond to the edge of a bar are missing, although the resolution of the C+D-array data is too low to resolve the inner bar identified in Figure 5. In addition, the velocity field anomalies that we do see are not associated with the optical galaxy. The velocity field of the C-array data shows more variations everywhere, probably because of the lower signal-to-noise. And, in the C-array velocity field there is an anomaly at the southwest end of the inner bar, but this is also where the supergiant H II complex NGC 2363 is located and it is expected to have an impact on the surrounding interstellar medium (ISM) there. Thus, we see no velocity field anomalies that we can convincingly associate with a bar structure.

A bar in NGC 2366 could be more subtle, however. NGC 2366 is a later type galaxy than is usually studied for bar flows, so we might not see the same kinematic features that are found in other galaxies. The LMC, for example, is a small system like NGC 2366, and it has a clear optical bar, but this bar has virtually no signature in the HI intensity and only a mild distortion of the inner HI velocity fields (Kim et al. 1998). In this sense, it resembles NGC 2366. In addition, many late type galaxies tend to look elongated or irregular in outline like NGC 2366, so it is possible that some of the observed ellipticity in Figures 4 and 5 is the result of an intrinsically prolate structure. If this is the case, then what should we expect for non-circular perturbations in the velocity field?

Figure 4 in Athanassoula (1992) shows a model simulation that could be like part of NGC 2366. It is for a barred galaxy with no inner Lindblad resonance (ILR), and it shows a compressed central dust lane that runs almost like a straight line from each end of the bar through the nucleus. The bar compression does not take the form of two offset dust-lanes with an inner spiral, as in

earlier-type galaxies with an ILR. A straight dust lane in NGC 2366 could account for the central ridge of star formation in Figure 5 and for the thin inner HI and H α streaks in Figure 14. Another model with nearly straight dust lanes has a large bar axial ratio (Fig. 6 in Athanassoula 1992). Such axial ratios also result from the lack of an ILR.

NGC 2366 has a solid body rotation curve in the inner part, as shown in Figure 17. This implies that the value of $\Omega - \kappa/2$, where Ω is the angular rotatino rate and κ is the epicyclic frequency, is nearly zero there and makes it unlikely there is an ILR, which requires $\Omega - \kappa/2$ to equal the rotation speed Ω . Thus, the Athanassoula simulation seems relevant to NGC 2366.

The velocities in the Athanassoula (1992) solutions are parallel to the bar in the inner regions, with a convergence and shock near the bar major axis. Such velocities would twist the HI minor kinematic axis away from the optical minor axis in a manner like that seen in Figures 16 and 18 (middle panel).

For example, the southwest side of NGC 2366 is approaching us, so the counter-clockwise twist of the velocity contours in the inner region (compared with the minor isophotal axis) indicates more of the same approaching motions to the west of the center than in the east. If NGC 2366 rotates counter-clockwise, so that the near side is in the northwest, then this twist is consistent with a bar whose far end is toward the south, and whose parallel approaching streaming motions are from the far side to the near side in the western part of the disk. In this case, the bar would be twisted slightly clockwise compared to the major axis of the outer part of NGC 2366. Alternatively, if NGC 2366 rotated clockwise (placing the near side in the southeast), then the observed twist of the velocity contours would be consistent with a bar whose far end is toward the north, and whose parallel streaming motions are from the far side to the near side in the same western part of the disk. In this case also, the bar would be twisted slightly clockwise from the major isophotal axis of NGC 2366. In both cases, we should look for an optical bar that is slightly offset in the clockwise direction from the orientation of the outer part of NGC 2366. This offset might be seen in Figure 5. The contour level at 24.04 mag arcsec⁻² shows a twist of the faint optical light in this sense, extending for the same radius as the counter-clockwise twist of the HI velocity contours in Figure 18.

5.6. Velocity Dispersion

A false-color display of the velocity dispersion map is shown in Figure 18. Within the confines of the optical galaxy, the velocity dispersion of the HI gas is mostly $12-20 \text{ km s}^{-1}$ seen in the C+D-array map. This is high compared to the canonical value of 10 km s^{-1} found in the quiescent gas of many galaxies including irregulars. In the higher resolution C-array velocity dispersion map, however, we see that most of the HI disk is in fact at $5-10 \text{ km s}^{-1}$ dispersion but that the HI ring, including regions without star formation, has dispersions of $10-17 \text{ km s}^{-1}$.

Figure 18 shows a comparison of the velocity dispersion to the V-band and $H\alpha$, the velocity

field, and the integrated HI by superposing contours in three displays. One can see that there are regions of high velocity dispersion, 20–30 km s⁻¹, scattered around the HI disk. One would expect the velocity dispersion of the neutral gas to be high in regions of star formation. In the supergiant H II regions in particular, where there is intense star formation, the ionized gas itself is known to have high velocity dispersions (Hunter 1982; Hunter & Gallagher 1990, 1992, 1997). However, Figure 18 shows that the regions with the highest velocity dispersions in HI are found outside the regions of star formation and beyond the bright part of the optical galaxy altogether. In fact the high velocity dispersions are not associated with any obvious feature in the optical or HI. The only exception is that an "arm" of higher velocity dispersion curves around the northern and western sides of the "knob" of HI in the northeast part of the galaxy (see bottom panel of Figure 18 and Figure 12).

Some regions of high velocity dispersion occur where the velocity contours crowd together, as illustrated in the middle panel of Figure 18. This is true particularly in the northwest region, where the contours are vertical $(7^h \ 23^m \ 13.4^s, \ 69^\circ \ 21' \ 07'')$. In this case, part of the high dispersion comes from unresolved systematic motions. However, in other cases the contribution from rotational motions is small. For example, profiles of the region of high velocity dispersion to the east of the center of the galaxy $(7^h \ 24^m \ 00.6^s, \ 69^\circ \ 18' \ 32'')$ are shown in Figure 19. The line profiles in these regions are simply very broad and in some places double peaked.

The regions of high velocity dispersion not significantly affected by the velocity gradient, especially the spiral-like features in the outer parts of the disk, are more difficult to explain. They could have a turbulent origin. Figure 20 shows scans of column density as dashed lines and velocity dispersion as solid lines, taken across the entire disk from east to west. Each scan is averaged in vertical bands that are one beam FWHM wide. They go through three main regions of high velocity dispersion, which are at the indicated positions: E $(7^h24^m00.6^s, 69^\circ18'32'')$, N $(7^h23^m38.9^s, 69^\circ20'52''$; includes the northwest region as well), and SW $(7^h22^m58.4^s, 69^\circ16'57'')$. The figure shows a tendency for the velocity dispersion to increase where the column density decreases. There is nearly a one-to-one correspondence between these opposing variations in the central regions of the galaxy. This suggests a process where there is some pressure or wave-like communication between the regions. Low density regions have greater wave or turbulent motions than high density regions, in a manner analogous to the turbulent motions in individual clouds.

Another factor that can affect line profiles is low signal-to-noise, and the regions with high velocity dispersion are also regions of low HI column density. It is claimed that noisier profiles, such as one might expect in low intensity regions, will appear broader. If this were the explanation of the high c regions that we see here, then we would expect all regions in the outer parts of the galaxy to have high c. Yet, in Figure 18 we see a few selected regions only with anomolously high c. Furthermore, Figure 19 shows the profiles in one of these regions, and they are clearly broad even though noisy. Thus, while this effect may be entering in at some level, we believe that these regions of anomolously high c and the trend we see in Figure 20 are real.

This anti-correlation between velocity dispersion and HI column density that we find in NGC 2366 is different from what is seen in the Scd galaxy IC 342. There, over most of the galactic disk c is highest where the gas column density is highest (Crosthwaite, Turner, & Ho 2000). The exception in IC 342 is the center where c peaks and the HI column density drops. Crosthwaite et al. suggest that in the center of IC 342 some additional gas component is contributing to the total gas surface density. Elsewhere in IC 342, the correlation between the surface density and velocity dispersion suggests there is a local source of turbulent energy from gas compression in a density wave or local spiral instability. In NGC 2366, there are apparently no analogous spiral instabilities.

However, there is another situation in which there is an anti-correlation between a velocity dispersion and HI column density. That is in the irregular galaxy NGC 4214. In a comparison of H α and HI velocity fields in that galaxy, Wilcots & Thurow (2001) found that the highest H α velocities are those of the diffuse ionized gas, often in regions of low HI column density and holes. They argue that these are the signatures of outflows fueled by surrounding concentrations of massive stars and accelerated by the steep density gradients into holes. However, this seems unlikely to explain the regions of high c in the HI in NGC 2366. Although the regions of high c in NGC 2366 are located in the outer parts of the galaxy where there is a general density gradient, there are not the concentrations of large numbers of massive stars nearby that are seen in NGC 4214 to supply the mechanical energy input. The exception is NGC 2363, of course, but there are pockets of high c in NGC 2366 located on the other side of the galaxy from NGC 2363. Furthermore, in this scenario the high velocity dispersion is in the *ionized* gas, not the neutral gas, since the massive stars are ionizing the medium as well.

5.7. HI and NGC 2363

The current star formation activity of NGC 2366 is dominated by the supergiant H II complex NGC 2363, the scale of which is truly remarkable (Kennicutt, Balick, & Heckman 1980). Star formation appears to have been continuing over a period of time up to 10 Myr throughout the complex. There is spectroscopic evidence of the presence of Wolf-Rayet stars, indicating an age of 3–5 Myr, if they are normal evolved massive stars, near the brightest part of the nebula (Drissen, Roy, & Moffat 1993; González-Delgado et al. 1994). Star formation over periods of order 10 Myr is also what is observed in large H II complexes in the LMC such as 30 Doradus or Constellation III (see, for example, discussion by Dolphin & Hunter [1998] and references therein).

NGC 2363 also has a system of H α arcs that form a partial shell 835 pc long along the northeast perimeter of the H II complex (Figure 21). If they represent a shell centered on the brightest nebula in the complex, the diameter of the shell would be 1500 pc (Hunter & Gallagher 1990). Spectroscopy shows that the arcs are photoionized (Hunter & Gallagher 1997). In addition to the arcs, there are diffuse filaments of ionized gas 2–5 times lower in surface brightness that extend from the western-most end of the arcs to the northwest away from the nebula (Hunter,

Hawley, & Gallagher 1993). These filaments are of order 770 pc long and 60 pc wide. They extend to 1130 pc from the center of NGC 2363.

Furthermore, high velocity ionized gas with FWHM of 38 km s⁻¹ and FWZI of 190 km s⁻¹ is associated with the nebula; the ionized gas alone has a kinetic energy of 9×10^{50} ergs s⁻¹ (Hunter 1982, Roy et al. 1992, Hunter & Gallagher 1997, Martin 1998). Roy et al. (1991) argue that there is a 285 pc diameter bubble of gas expanding at 45 km s⁻¹ in the nebula. All of this motion of the ionized gas is most certainly a consequence of the concentration of massive stars in the complex. Evidence is seen for at least one supernova remnant (Yang, Skillman, & Sramek 1994).

We have examined the HI within and around NGC 2363 to look for any relationship to the ionized gas structures and unusual activity in the gas. In Figure 21 we show our H α image of NGC 2363. One can see the arcs of the partial shell curving around the HII region to the northeast and the faint, diffuse filaments trailing away from the nebula to the northwest. There is also diffuse H α emission to the west between NGC 2363 and the giant HII region to the west (numbered III by Drissen et al. 2000). Contours are superposed on the H α image from the higher resolution C-array integrated HI map. One can see that the HII region is offset from the HI peak, as is commonly seen (for example, Sextans A: Hodge, Kennicutt, & Strobel 1994). The H α peak is 18" (300 pc), about one HI beam-width, to the west of the HI peak. The faint, diffuse filaments to the northwest are entering a region that is a local HI minimum as would be expected if they are part of a champagne flow away from the gas cloud. The ionized gas arcs to the northeast, on the other hand, cross the HI ridge and there are two minor HI peaks located along the shell as well. Where the ridge of HI ends as one moves to the northwest along the arcs is where the arcs end and the faint, diffuse filaments begin.

Kinematically there is some anomaly in the C-array velocity field at NGC 2363. This can be seen in Figure 22 where we show contours of the velocity field superposed on our $H\alpha$ image. In the vicinity of the $H\alpha$ arcs on the northeast side of NGC 2363 the velocities of the HI are lower than one would expect except for a small pocket were the velocities are higher. However, the magnitude of these variations is of order 5 km s⁻¹, which is less than the velocity dispersion of the gas. In Figure 23 we show line profiles across the NGC 2363 region and immediate vicinity. Although a few line profiles are double, most are not. Furthermore, the FWHM of the line profiles in the H II region, in the arcs, and in the diffuse filaments are comparable to what is seen throughout the galaxy.

5.8. Shells

Holes and shells have been found in the HI distributions of various irregular galaxies. Most shells within the optical galaxy are believed to be the consequence of the energy input from massive stars that have recently formed, although non-stellar explanations have been proposed for larger holes, especially those outside the optical galaxy (Wada, Spaans, & Kim 2000). Shells

are seen in the HI distributions of galaxies such as DDO 50 (Puche et al. 1992), IC 10 (Wilcots & Miller 1998), and the LMC (Kim et al. 1999). In those galaxies the shells are apparent in the integrated HI maps. We do not see evidence of shells in our integrated map of NGC 2366, nor in a careful examination of channel maps and position-velocity plots. Of the 51 shells catalogued in DDO 50 by Puche et al. the diameter ranges from 140 to 1900 pc with an average of 730 ± 440 pc. The average size in IC 10 is 160 ± 40 pc (Wilcots & Miller 1998). If shells were present in NGC 2366, our resolution of 300 pc×220 pc (C-array map) should have allowed us to detect the largest structures found in DDO 50. However, NGC 2366 could contain numerous more modest-sized shells that we would not be able to resolve with these data.

5.9. The Suggestion of an Interaction Considered

Drissen et al. (2000) have suggested that H II region number III to the west of NGC 2363 and the ridge of gas that it sits on are actually a satellite galaxy now interacting with NGC 2366. They base this idea on the age sequence running from east to west through the NGC 2363 star-forming complex and suggest that the interaction initiated star formation in this region which then spread in a sequential manner. However, as we have seen, the HI, although having significant peculiarities, is not as peculiar as one might expect in the case of an on-going merger. Morphologically, the two ridges of gas deproject into a lumpy ring of gas that is not particularly unusual in appearance. Further, in this ring the gas complex associated with region III does not stand out as particularly unusual compared to the NGC 2363 complex. Kinematically, we have noted that there are large-scale peculiarities: the position angle of the kinematical axis is rotated from those of the optical and HI morphology, there is gas extending southwest of NGC 2363 at unusual velocities, and the isovelocity contours on the west side of the galaxy rotate to become almost north-south. However, we do not see evidence of gas at unusual velocities specifically associated with region III. Futhermore, similar peculiarities are found in many other galaxies. Thus, while it is possible that the velocity field peculiarities do indicate that NGC 2366 has been disturbed by an outside force sometime in the past, we do not feel compelled by the data to assign HII region III outsider status at this time.

6. Star Formation in NGC 2366

There is evidence for an empirical dependence for local star formation activity within a galaxy that involves a threshold. In a thin, differentially-rotating disk composed of pure gas (Safronov 1960) or stars only (Toomre 1964), there is a critical surface density Σ_c above which the disk is unstable to ring-like perturbations in the radial direction. Kennicutt (1989) calculated the critical gas density in this model (Quirk 1972) for a sample of normal Sc spiral galaxies. He found that the ratio of observed gas density Σ_g to critical gas density Σ_c typically exceeds 1 at mid-radius in the optical disk, and then falls with increasing distance from the center of the galaxy; star

formation was not detected beyond the point where Σ_g/Σ_c dropped below 0.7±0.2. He concluded that in Sc galaxies places where $\Sigma_g/\Sigma_c<0.7$ are too stable to form stars; interior to this, the gas density exceeds the local threshold for star formation.

Motivated by the apparent success of the gravitational instabilities model for spiral galaxies, we explored the applicability of several models to a small sample of irregular galaxies (Hunter, Elmegreen, & Baker 1998; see also Hunter & Plummer 1996, Meurer et al. 1996, van Zee et al. 1997). These models included (1) thin-disk, single-fluid gravitational instabilities, (2) thick-disk, two-fluid (stars+gas) gravitational instabilities, (3) three-dimensional gravitational instabilities based on a comparison between the local gas volume density and the local galactic virial density, (4) gravitational instabilities limited by the shear time, which uses a modified Σ_c based on the Ourt shear constant A instead of the epicyclic frequency κ , (5) the two-phase thermal properties of the ISM, and (6) any of a variety of models, presumably based on triggering or feedback, in which the star formation rate depends on the local stellar density. In addition, we also considered all of these models in a second case where the relative density of dark matter is high in the disks of irregular galaxies, as motivated by the high relative dark matter densities overall (e.g. Carignan & Beaulieu 1989). The resulting critical densities for cloud formation for each of these models were compared with the observed gas surface densities. The ratio of observed to critical gas density as a function of radius was also compared with the azimuthally-averaged current star formation rate and with the V-band stellar surface brightness, a tracer of star formation integrated over a timescale of ~ 1 Gyr.

We found that the thin-disk, single-fluid model that works so well for spirals does not work for irregulars. We found that the ratios of observed to critical gas densities are lower in irregulars than in spiral galaxies by a factor of ~ 2 in all cases but the shear-regulated model, suggesting that the gas is highly stable on large scales against cloud formation. The absolute criterion based on this model, therefore, predicts that star formation should not be occurring at all in irregulars. In addition, the relative criterion as a function of radius does not predict the observed star formation edge in the galaxies, nor does it predict the variation in star formation rate from galaxy to galaxy.

In Figure 24 we show this failure of the models for NGC 2366 as well. There we plot the deprojected surface densities Σ_g and the Σ_c for the thin rotating disk gravitational instability model. The values of Σ_g have been determined from Σ_{HI} , assuming the kinematically-determined inclination of 65°. If one were to use the inclination of 72° suggested by the morphology, the dominant effect is the $\cos(i)$ in deprojecting the column densities. In that case the measured surface densities decrease by a factor of \sim 0.7. In addition Σ_{HI} has been corrected for He $(0.34\times\Sigma_{HI})$. Including molecular gas is far more difficult; few irregular galaxies have been adequately mapped, so the spatial distribution of H_2 is not generally known. Instead, we took a globally averaged M_{H_2}/M_{HI} ratio and simply multiplied the HI everywhere by this in order to statistically include H_2 . For the M_{H_2}/M_{HI} ratio we used an average between the SMC, where molecular gas is 7% of the HI gas content (Rubio et al. 1991), and the LMC, where the ratio is 30% (Cohen et al. 1988). That is, the H_2 content was taken to be $0.18\times\Sigma_{HI}$. This correction for

the presence of H_2 is clearly unsatisfactory, but at present there is no better information on these galaxies. Thus, we took Σ_g to be $1.52 \times \Sigma_{HI}$.

 Σ_c was determined from $\Sigma_c = \frac{\kappa c}{3.36G}$, where κ is the epicyclic frequency and c is the velocity dispersion of the gas. We determined c as a function of radius by integrating the velocity dispersion map in ellipses of 25" width and using a position angle of 46° and an inclination angle of 65°. The mean velocity dispersion in these ellipses, determined from the C+D-array map, is about 16 km s⁻¹ out to a radius of 5', and declines slowly from there to 10 km s⁻¹ at a radius of 11.7'. The values of Σ_g/Σ_c in NGC 2366 are typical of the irregulars in our previous study: The maximum in Σ_g/Σ_c , 0.5, is still below the star formation cut-off value of 0.7 found by Kennicutt (1989) for spirals.

These failures of the models suggest that other processes are important for cloud and star formation in irregulars, leading us to suggest more local effects. An obvious mechanism is sequentially triggered star formation driven by the mechanical energy input from concentrations of massive stars resulting in gas density irregularities. Another process is random gas compression from turbulence. Kinematics in Im systems are often dominated by random gas motions which can contribute significantly to the pressure (for example, Gottesman & Weliachew 1977; Tully et al. 1978; Huchtmeier et al. 1981; Sargent, Sancisi, & Lo 1983; Lo, Sargent, & Young 1993; Feitzinger et al. 1981), and in some cases rotation can be insignificant compared to random motions (Young & Lo 1996). Both of these processes have a sensitivity to the critical density like the gravitational instability model, but do not involve large-scale instabilities directly. They could in fact dominate the star formation process when spiral arms are not present or are weak (see also Thornley & Wilson 1995). Further evidence that local inhomogeneities in the gas may dominate the star formation process come from the observations that H II regions are found near peaks in the gas even when the azimuthally-averaged gas is below the critical threshold density (van der Hulst et al. 1993; van Zee et al. 1997; Meurer et al. 1998).

Because of the apparent dominance of local inhomogeneities in the gas distribution, we have determined the maximum Σ_g at the positions of the H II regions in NGC 2366, $\Sigma_g(\text{max})$. As for Σ_g , $\Sigma_g(\text{max})$ uses an inclination angle of 65° to convert from column density to surface density and is corrected to account for the presence of He and, statistically, H₂. We have determined the maxima using the C-array maps for the higher spatial resolution (300 pc×220 pc) they give and have looked for the HI peaks within a beam area or the diameter of the H II region, whichever was larger. For most H II regions the beam-size is larger than the H II region diameter. This does not take into account the possibility that the H II region is offset from the gas cloud out of which it has formed, nor can it account for destruction of the cloud since the formation of the H II region. The values of $\Sigma_g(\text{max})$ at each H II region are shown in Figure 24 along with the Σ_c from the thin-disk instability model and the azimuthally-averaged Σ_g . We see that the $\Sigma_g(\text{max})$ cover a relatively small range, 18–36 M_{\odot} pc⁻², except in the center (<0.5R₂₅) and outer (>1.75R₂₅) galaxy where $\Sigma_g(\text{max})$ are lower. In fact, the $\Sigma_g(\text{max})$ are comparable to the annular Σ_g in the inner 0.5R₂₅ of the galaxy, but beyond ~0.75R₂₅ the $\Sigma_g(\text{max})$ are roughly comparable to Σ_c . The transition

region corresponds roughly to the radius at which the rotation of the galaxy ceases to be that of a solid body (inner vertical dashed line). Also, star formation does not extend very much beyond the radius where the rotation curve begins to fall (outer vertical dashed line).

The rise and fall of $\Sigma_g(\max)$ is similar to the rise and fall of the limiting tidal density in the disk midplane. The tidal density is

$$\rho_T = -\frac{3\Omega R}{2\pi G} \frac{d\Omega}{dR} \tag{1}$$

for angular rotation rate Ω and radius R. In the rising part of the rotation curve, $d\Omega/dR$ is small so ρ_T is small, and in the flat part of the rotation curve, ρ_T decreases as $1/R^2$. To compare this with the observations, we have to convert ρ_T into a tidal-limit surface density, Σ_T . We multiply ρ_T by twice the scale height, $H = c/(2\pi G \rho_T)^{0.5}$ to get

$$\Sigma_T = \frac{\Omega c}{\pi G} \left(-3d \ln \Omega / d \ln R \right)^{0.5} \tag{2}$$

for velocity dispersion c. This quantity, corrected for the presence of He and H₂ as for Σ_g , is plotted in Figure 24 as crosses. The general agreement of Σ_T with $\Sigma_g(\max)$ indicates that the peak column densities near the HII regions are not particularly dense, but only at about the tidal limit. Lower density clouds should not bind themselves together well. The tidal limit in the flat part of the rotation curve is higher than the peak column density, but this is probably a result of our not including stars in the expression for H. If we write $H = c/\left[2\pi G\left(\rho_T + \rho_{stars}\right)\right]^{0.5}$, then the tidal limit equals the observed $\Sigma_g(\max)$ if $\rho_{stars} \sim 0.6 \rho_{gas}$. Stars in the inner disk lower Σ_T too, making the clouds there relatively more self-bound.

Various people have suggested that, rather than a varying critical density stability criterion, there is a simple constant and universal density threshold for star formation (Gallagher & Hunter 1984; Skillman 1987; Taylor et al. 1994; Meurer et al. 1996; Hunter et al. 1998; van Zee et al. 1998). Most estimates for this threshold are observed column densities of $\sim 10^{21}$ atoms cm⁻², which corresponds to an HI surface density (corrected for inclination of the galaxy) of 3 $\rm M_{\odot}~pc^{-2}$ in NGC 2366 or $\rm \Sigma_g$ of 5 $\rm M_{\odot}~pc^{-2}$ corrected for He and H₂. We had also estimated a critical gas density of 3 $\rm M_{\odot}~pc^{-2}$ from azimuthally-averaged $\rm \Sigma_g$ for a sample of irregulars. In NGC 2366 we see that all of the star formation is taking place at surface densities $\rm \Sigma_g(max){>}6~M_{\odot}~pc^{-2}$ or at an azimuthally-averaged $\rm \Sigma_g{>}3~M_{\odot}~pc^{-2}$, and the bulk of it is taking place at >15 $\rm M_{\odot}~pc^{-2}$. The data for NGC 2366 are not inconsistent with this simple, universal threshold.

Additional support for this universal threshold comes from comparing peak column densities in galaxies with different levels of star formation activity. The caveat, as always, is that the measured column densities depend on the beam-size of the observations relative to the size of the galaxy. Nevertheless, they can give us some indication of differences between galaxies. In our larger sample of irregulars assembled for purposes of studying star formation processes, there are four galaxies with no measurable star formation activity (determined from H α images) and with published HI maps given with contour levels. In these four galaxies the highest observed HI contours are column densities of 1–7×10²⁰ atoms cm⁻² (LGS3–Young & Lo 1997;

M81dwA–Sargent et al. 1983; F564-V3 and F567-2–de Blok, McGaugh, & van der Hulst 1996). These column densities correspond to deprojected HI surface densities of $0.8–5~\rm M_{\odot}~pc^{-2}$ for these galaxies. There are also three galaxies in this sample with star formation rates per unit area less than $10^{-4}~\rm M_{\odot}~yr^{-1}~kpc^{-2}$, the lowest non-zero rates measured in this sample, and they have HI contour levels shown to $7–24\times10^{20}~\rm atoms~cm^{-2}$ (DDO 52–Simpson 1995; DDO 69–Young & Lo 1996, note the factor of two difference in N_{HI} for the two beam sizes that they give; DDO 216–Lo et al. 1993). These column densities correspond to HI surface densities of 2–10 $\rm M_{\odot}~pc^{-2}$. Of three galaxies with somewhat higher star formation rates— 10^{-3} – $10^{-4}~\rm M_{\odot}~yr^{-1}~kpc^{-2}$, the highest HI contours are $7–14\times10^{20}~\rm atoms~cm^{-2}$ (DDO 105–Broeils 1992; F563-1 and F565-V2–de Blok et al. 1996). These column densities correspond to HI surface densities of 3–5 $\rm M_{\odot}~pc^{-2}$. The picture is not clean but suggests that something like an HI surface density of \sim 2–5 $\rm M_{\odot}~pc^{-2}$, or a $\rm \Sigma_{\it g}$, corrected for He and H₂, of 3–8 $\rm M_{\odot}~pc^{-2}$ could be a universal cutoff for massive star formation. Of course, these estimates are based on looking at the contours that enclose the bulk of the star formation and do not refer to the peaks in $\rm \Sigma_{\it g}$.

There is good reason for an absolute minimum surface density threshold in irregular galaxies, in addition to whatever other thresholds there might be, and this is the requirement of a cool phase of HI as a precursor to star formation. The existence of a cool phase depends on the pressure and radiation field. For normal radiation fields in star-forming disks, the pressure has to exceed several times 10^3 K cm⁻³ for the HI to allow an equilibrium cool phase. This pressure comes entirely from the disk self-gravity, and depends on the square of the column density. For a Σ_g of 8 M_{\odot} pc⁻², the pressure is $(\pi/2) G\Sigma_g^2 \sim 2000$ K cm⁻³. Lower column-density regions should have their HI only in the warm, low-density phase (Elmegreen & Parravano 1994; Braun 1997).

While it is clear that star formation is dependent on local gas peaks to form stars, to some extent this is a circular argument. We know that star formation begins with the formation of a gas cloud, and so it is not at all surprising that local peaks in the gas are where we find H II regions. Once a gas cloud forms and reaches a certain density, it forms stars. The larger question is what causes those clouds to form in the first place in irregular galaxies. Large-scale gravitational instabilities do not seem to operate with the same vigor as in giant spiral galaxies, because the gas has a lower ratio of Σ_g/Σ_c by a factor of 2. Another mechanism could take over in the absence of strong self-gravity, and that is the rearrangement of gas by the input of mechanical energy from concentrations of massive stars in previous episodes of star formation. This is the Stochastic Self-Propagating Star Formation (SSPSF) model of Gerola, Seiden, & Schulman (1980; Wada, Spaans, & Kim 2000), based on complex feedback and triggering scenarios.

In NGC 2366 Aparicio et al. (1995) argue that there is no large-scale propagation between regions seen in color-magnitude diagrams of the stellar populations. However, their CCD images did not include the redder regions of the galaxy that we see in Figure 9. The redder stellar population situated in the center of the HI ring which now hosts most of the star formation activity of the galaxy does suggest some sort of propagation from a central point outward. This is similar to what is seen in the irregular galaxy Sextans A (=DDO 75): The center of Sextans

A, where there is an HI minimum, is dominated by older stars (Hoessel, Schommer, & Danielson 1983; Aparicio et al. 1987; Dohm-Palmer et al. 1997). Outside of the center, the bulk of the star formation is taking place in regions associated with two large HI complexes (Skillman et al. 1988).

Without a previous generation of stars, star formation still had to begin somehow, and perhaps this is where gravitational instabilities contribute. Even with a low ratio Σ_g/Σ_c , instabilities can still operate when there is energy dissipation (Elmegreen 1991; Elmegreen 1995; Gammie 1996), but they operate relatively slowly, at the viscous rate. This type of slow instability might be more important for irregulars than spirals, because the lack of competition from shear in irregulars means there is a lot of time available. Indeed, most of the visible disk of NGC 2366 has virtually no shear, so cloud-forming instabilities can take a very long time to develop.

Dohm-Palmer et al. (1998) in a study of the stellar populations in the irregular galaxy DDO 155 (=GR8) noted that the recent star formation is concentrated near the main HI complexes. They argue that the HI complexes are long-lived objects and that star formation takes place within them over hundreds of Myr without destroying the complexes. The giant complex NGC 2363 could be long-lived too, but the similarity of the peak HI density to the critical tidal density in Figure 24 implies that NGC 2366, like the other star-forming regions, is not tightly self-bound on a large scale. A good test of this hypothesis would come from the star formation history of this complex. If there is a population of stars dating back several hundred million years that is exclusively in NGC 2363, then the complex may be relatively long lived.

7. Summary

We have presented deep UBVJHKH α images and HI maps of NGC 2366. We see that the galaxy is a boxy-shaped structure at relatively high inclination. The optical morphology suggests several bar structures including one in which the whole galaxy is a bar. However, there is only a weak observational signature of a bar potential in NGC 2366. There is an asymmetrical extension of stars along the southwest end of the major axis of the galaxy, and this is where the furthest star-forming regions are found, at a radius of $1.3R_H$. The colors of the galaxy are approximately constant with radius when averaged azimuthally, but show large-scale structure in ratio images. The center of the HI ring and a low surface brightness region to the northeast appear to be redder than the rest of the galaxy. The optical surface photometry is fit with an exponential disk that also applies to the near-infrared surface photometry. The scale length and central surface brightness of the disk are normal for late-type galaxies.

The star formation activity of the galaxy is dominated by the supergiant H II complex NGC 2363 that contains 70% of the total H α luminosity of the galaxy. The global star formation rate for NGC 2366 is, however, only slightly elevated for an Im system, and there is enough gas to last another one or two Hubble times at the current rate. The star formation activity drops off with radius approximately as does the starlight until the outer part of the galaxy is reached and then it

drops faster.

We detected HI to a radius of $2.3R_H$ at 1.7×10^{19} atoms cm⁻². The integrated HI shows two ridges running parallel to the major axis that when deprojected appear as a ring of diameter 5.5 kpc with a central depression and a somewhat redder stellar population, as is seen in some other irregulars. Most of the star formation is found along the eastern of the two ridges, but one major H II complex is on the western ridge. The HI is not centered symmetrically on the optical galaxy. The azimuthally-averaged surface density of HI is comparable to that of other irregulars in the inner part of the galaxy but drops off slower and extends further in the outer parts. Globally, NGC 2366 is more gas-rich than other irregulars.

The kinematics of the HI are not those of a well-behaved rotating disk. The velocity field to the southeast of the center of the galaxy and along the western edge especially deviate from a model rotating disk. There could be a weak kinematic signature of a bar tilted clockwise relative to the major axis of the galaxy by a few tens of degrees. The inclination and position angles derived from the kinematics differ from those derived from the optical and HI morphology by 7–22°. There are regions of unusually high velocity dispersion, but these regions are not associated with the optical galaxy or features in the HI. Most regions of high velocity dispersion correspond instead to regions of slightly depressed HI column density, as if there is some continuity from region to region in the turbulent pressure and wave motions of the interstellar medium. Within the confines of the optical galaxy, the velocity dispersion is higher in the HI ring than in the surrounding disk. HI clouds have properties like those of clouds in other luminous irregulars. We did not detect any shell structures in the HI. The HI around the star-forming complex NGC 2363 is fairly unremarkable with a small velocity anomaly in the vicinity of the H α arcs, and the large ionized gas shell appears to be perpendicular to the HI ridge containing the complex.

Like in other disk galaxies, the gas in NGC 2366 is lumpy and star-forming regions are associated with these lumps. H II regions are found where the gas surface densities locally exceed $6~\rm M_{\odot}~pc^{-2}$. What causes these clouds to form in the first place? NGC 2366, like other irregulars, has low gas densities relative to the critical gas densities of gravitational instability models, so large-scale gravitational instabilities would operate slowly or not at all. Such a slowness of cloud-forming instabilities may not be as much of a problem for irregular galaxies as it is for giant spirals because of the lack of shear in the irregulars. When shear is low, there is little competition to the growth of giant cloud complexes following turbulent energy dissipation.

DAH is very appreciative of the travel support and hospitality of the Kapteyn Astronomical Institute that enabled her to travel to the Kapteyn Laboratory in Groningen where she received invaluable tutoring in the analysis of HI-interferometric data and the use of GIPSY. We thank A. Tomita for a critical reading of the manuscript. We appreciate the use of Ohio State University's Fabry-Perot and the Ohio State Infrared Imager-Spectrograph and Mark Wagner for making them work for us. Support to DAH for this research came from the Lowell Research Fund and grant AST-9802193 from the National Science Foundation; support to BGE came from grant

AST-9870112 from the National Science Foundation.

Table 1. Continuum Objects in the Field.

Object	Flux (Jy)	RA (1950)	DEC (1950)	FWHM ^a (")
NGC 2363	0.024	$7^h \ 23^m \ 25.2^s$	69° 17′ 30″	
1	0.053	$7^h \ 19^m \ 30.8^s$	$69^{\circ}~20'~15''$	38
2	0.009	$7^h \ 20^m \ 43.0^s$	$69^{\circ}~23'~25''$	43
3	0.012	$7^h \ 20^m \ 59.1^s$	$69^{\circ}\ 15'\ 18''$	35
4	0.027	$7^h \ 21^m \ 05.5^s$	$68^{\circ} 59' 02''$	
5	0.022	$7^h \ 21^m \ 54.0^s$	$69^{\circ}\ 25'\ 28''$	41
6	0.012	$7^h \ 22^m \ 04.4^s$	$69^{\circ}~30'~01''$	40
7	0.002	$7^h \ 22^m \ 29.2^s$	$69^{\circ}\ 20'\ 57''$	
8	0.179	$7^h \ 22^m \ 39.2^s$	68° $58'$ $57''$	38
9	0.012	$7^h \ 22^m \ 40.6^s$	$69^{\circ}~36'~49''$	39
10	0.069	$7^h \ 23^m \ 14.9^s$	68° $57'$ $54''$	37
11	0.052	$7^h \ 23^m \ 14.9^s$	$68^{\circ} 56' 50''$	43
12	0.008	$7^h \ 24^m \ 35.2^s$	68° $59'$ $13''$	39
13	0.047	$7^h \ 24^m \ 55.3^s$	$69^\circ\ 35'\ 21''$	36
14	0.014	$7^h \ 25^m \ 07.3^s$	69° $12'$ $00''$	36
15	0.012	$7^h \ 25^m \ 25.7^s$	$69^{\circ}\ 16'\ 24''$	38
16	0.005	$7^h \ 25^m \ 28.3^s$	69° $11'$ $20''$	35
17	0.044	$7^h \ 26^m \ 22.7^s$	$69^{\circ}\ 25'\ 49''$	37
18	0.010	$7^h \ 26^m \ 20.3^s$	$69^\circ\ 31'\ 01''$	31
19	0.085	$7^h \ 27^m \ 14.0^s$	$69^{\circ} \ 06' \ 01''$	37
20	0.077	$7^h \ 28^m \ 00.8^s$	$69^{\circ}\ 15'\ 33''$	49

 $^{\mathrm{a}}$ We include the FWHM of the objects in the continuum image by request, but bear in mind that the beam FWHM is $34'' \times 29''$ and so most of these objects are unresolved.

Table 2. Position Angles and Inclinations.

Component	a ^a (')	a/R_{25}	PA (°)	b/a	i ^b (°)	Center (1950)	ΔRA (" E)	ΔDEC (" N)
Stars-outer isophote Stars-middle isophote	4.3 1.6	1.64 0.63	32.5 30	$0.42 \\ 0.27$	72 	7 ^h 23 ^m 30.9 ^s 69° 18′ 30″ 7 ^h 23 ^m 34.5 ^s 69° 18′ 38″	0 +19	0 +8
Stars-inner isophote	1.0	0.37	32	0.34		$7^h \ 23^m \ 37.2^s \ 69^\circ \ 19' \ 01''$	+33	+31
HI-morphology	7.9	3.02	23.5	0.41	73	$7^h \ 23^m \ 39.8^s \ 69^\circ \ 19' \ 24''$	+47	+54
HI–kinematics	> 2.5	> 0.96	46	• • •	65	$7^h \ 23^m \ 31.8^s \ 69^\circ \ 18' \ 47''$	+5	+17

^aSemi-major axis of the bar or, for the HI kinematics, radius at which the measurements apply.

 $^{{}^{\}mathrm{b}}\mathrm{Calculated}$ assuming an intrinsic b/a of 0.3.

Table 3. Summary of Global Optical, Near-IR, and HI Properties.

Parameter	Value
D (Mpc)	3.44
$M_{HI} (M_{\odot}) \dots \dots$	8.0×10^{8}
$E(B-V)_f^a$	0.043
$R_{25}^{b}(arcmin)$	2.6
$R_H^b(arcmin)$	5.1
μ_0 (V-band, magnitudes arcsec ⁻²)	22.82 ± 0.09
R_D (kpc)	1.59 ± 0.04
$M_{B,0} (R=7.4') \dots$	-16.51
$(U-B)_0 (R=7.4') \dots$	-0.40
$(B-V)_0 (R=7.4') \dots$	0.31
$M_{J,0} (R=4.0') \dots$	-17.53
$(J-H)_0 (R=2.6') \dots$	0.43
$(H-K)_0$ $(R=1.9')$	0.04
$\log L_{H\alpha,0} \text{ (ergs s}^{-1}) \dots$	40.27
SFR^{c} (M _{\odot} yr ⁻¹)	0.13
$\log SFR/area^{c} (M_{\odot} yr^{-1} kpc^{-2})$.	-2.22
$\mathrm{M}_{HI}/\mathrm{L}_{B} \; (\mathrm{M}_{\odot} \; / \mathrm{L}_{\odot} \;) \; \ldots \ldots$	1.36
$\mathrm{L}_{H(-0.5)}{}^{\mathrm{d}}\!(\mathrm{L}_{\odot})$	6×10^{7}
$M_{HI}/L_{H(-0.5)}^{d} (M_{\odot}/L_{\odot}) \dots$	13

 $^{a}E(B-V)_{f}$ is foreground reddening due to the Milky Way (Burstein & Heiles 1984). For the stars in NGC 2366, we assume a an additional internal reddening of 0.05 magnitude; for the H II regions we assume an additional internal reddening 0.1 magnitude (consistent with Balmer decrement observations of the emission nebula NGC 2363; see references in Table 7 of Hunter & Hoffman [2000]).

°Star formation rate derived from $L_{H\alpha}$ using the formula of Hunter & Gallagher (1986) that integrates from $0.1~\rm M_{\odot}$ to $100~\rm M_{\odot}$ with a Salpeter (1955) stellar initial mass function. The area is πR_{25}^2 .

 $^{^{\}rm b}{\rm At}$ NGC 2366 1'=1.0 kpc.

 $^{^{\}rm d}{\rm L}_{H(-0.5)}$ is measured within 0.316R₂₅, and ${\rm M}_{H\odot}{=}3.44.$

REFERENCES

Aaronson, M., Mould, J., & Huchra, J. 1980, ApJ, 237, 655

Aparicio, A., Cepa, J., Gallart, C., Castañeda, H. O., Chiosi, C., Bertelli, G., Mas-Hesse, J. M., Muñoz-Tuñón, C., Telles, E., Tenorio-Tagle, G., Diaz, A. I., García-Vargas, L. M., Garzón, F., González-Delgado, R. M., Pérez, E., Rodríguez-Espinosa, J. M., Terlevich, E., & Televich, R. J. 1995, AJ, 110, 212

Aparicio, A., García-Pelayo, J. M., Moles, M., & Melnick, J. 1987, A&AS, 71, 297

Athanassoula, E. 1992, MNRAS, 259, 345

Athanassoula, E., Morin, S., Wozniak, H., Puy, D., Pierce, M. J., Lombard, J., & Bosma, A. 1990, MNRAS, 245, 130

Bosma, A. 1981, AJ, 86, 1825

Bothun, G. D. 1984, ApJ, 277, 532

Braun, R. 1995, A&AS, 114, 409

Braun, R. 1997, ApJ, 484, 637

Broeils, A. H. 1992, Ph.D. Thesis, Univ. of Groningen

Broeils, A. H., & Rhee, M.-H. 1997, A&A, 324, 877

Broeils, A. H., & van Woerden, H. 1994, A&AS, 107, 129

Burstein, D., & Heiles, C. 1984, ApJS, 54, 33

Cardelli, J. A., Clayton, G. C., & Mathis, J. S. 1989, ApJ, 345, 245

Carignan, C., & Beaulieu, S. 1989, ApJ, 347, 760

Cayatte, V., Kotanyl, C., Balkowski, C., & van Gorkom, J. H. 1994, AJ, 107, 1003

Cohen, R. S., Dame, T. M., Garay, G., Montani, J., Rubio, M., & Thaddeus, P. 1988, ApJ, 331, L95

Combes, F., & Elmegreen, B. G. 1993, A&A, 271, 391

Crosthwaite, L. P., Turner, J. L., & Ho, P. T. P. 2000, AJ, 119, 1720

de Blok, W. J. G., McGaugh, S. S., & van der Hulst, J. M. 1996, MNRAS, 283, 18

de Jong, R. S. 1996, A&A, 313, 45

de Vaucouleurs, G., de Vaucouleurs, A., Corwin, H., Buta, R., Paturel, G., & Fouqué, P. 1991, Third Reference Catalogue of Bright Galaxies (New York, Springer-Verlag)

Dohm-Palmer, R. C., et al. 1997, AJ, 114, 2527

Dohm-Palmer, R. C., et al. 1998, AJ, 116, 1227

Dolphin, A. E., & Hunter, D. A. 1998, AJ, 116, 1275

Drissen, L., Roy, J.-R., & Moffat, A. F. J. 1993, AJ, 106, 1460

Drissen, L., Roy, J.-R., Robert, C., Devost, D., & Doyon, R. 2000, AJ, 119, 688

Elmegreen, B. G. 1991, ApJ, 378, 139

Elmegreen, B. G. 1995, in The 7th Guo Shoujing Summer School on Astrophysics: Molecular Clouds and Star Formation, ed. C. Yuan and Hunhan You, (Singapore: World Press), p 149

Elmegreen, B. G., & Elmegreen, D. M. 1985, ApJ, 288, 438

Elmegreen, B. G., Elmegreen, D. M., Chromey, F. R., Hasselbacher, D. A., & Bissell, B. A. 1996, AJ, 111, 2233

Elmegreen, B. G., & Hunter, D. A. 2000, ApJ, 540, 814

Elmegreen, B.G. & Parravano, A. 1994, ApJ, 435, L121

Elmegreen, D. M., & Elmegreen, B. G. 1980, AJ, 85, 1325

Feitzinger, J. V., Glassgold, A. E., Gerola, H., & Seiden, P. E. 1981, A&A, 98, 371

Gallagher, J. S., & Hunter, D. A. 1984, ARA&A, 22, 37

Gammie, C. F. 1996, ApJ, 462, 725

Gerola, H., Seiden, P. E., & Schulman, L. S. 1980, ApJ, 242, 517

González-Delgado, et al. 1994, ApJ, 437, 239

Gottesman, S. T., & Weliachew, L. 1977, A&A, 61, 523

Hodge, P. W., & Hitchcock, J. L. 1966, PASP, 78, 79

Hodge, P. W., Kennicutt, R. C., & Strobel, N. 1994, PASP, 106, 765

Hoessel, J. G., Schommer, R. A., & Danielson, G. E. 1983, ApJ, 274, 577

Honma, M., Sofue, Y., & Arimoto, N. 1995, A&A, 304, 1

Huchtmeier, W. K., Seiradakis, J. H., & Materne, J. H. 1981, A&A, 102, 134

Hunter, D. A. 1982, ApJ, 260, 81

Hunter, D. A. 1997, PASP, 109, 937

Hunter, D. A., Elmegreen, B. G., & Baker, A. L. 1998, ApJ, 493, 595

Hunter, D. A., & Gallagher, J. S. 1986, PASP, 98, 5

Hunter, D. A., & Gallagher, J. S. 1990, ApJ, 362, 480

Hunter, D. A., & Gallagher, J. S. 1992, ApJ, 391, L9

Hunter, D. A., & Gallagher, J. S. 1997, ApJ, 475, 65

Hunter, D. A., Gallagher, J. S., & Rautenkranz, D. 1982, ApJS, 49, 53

Hunter, D. A., Hawley, W. N., & Gallagher, J. S. 1993, AJ, 106, 1797

Hunter, D. A., & Hoffman, L. 2000, AJ, 117, 2789

Hunter, D. A., & Plummer, J. D. 1996, ApJ, 462 732

Hunter, D. A., van Woerden, H., & Gallagher, J. S. 1999, AJ, 118, 2184

Karachentseva, V. E., Karachentsev, I. D., & Börngen, F. 1985, A&AS, 60, 213

Kennicutt, R. C. 1984, ApJ, 287, 116

Kennicutt, R. C. 1989, ApJ, 344, 685

Kennicutt, R. C., Balick. B., & Heckman, T. 1980, PASP, 92, 134

Kennicutt, R. C., Tamblyn, P., & Congdon, C. W. 1994, ApJ, 435, 22

Kim, S., Staveley-Smith, L., Dopita, M. A., Freeman, K. C., Sault, R. J., Kesteven, M. J., & McConnell, D. 1998, ApJ, 503, 674

Kim, S., Dopita, M.A., Staveley-Smith, L., & Bessell, M.S. 1999, AJ, 118, 2797

Koribalski, B., Dettmar, R.-J., Mebold, U., & Wielebinski, R. 1996, A&A, 315, 71

Landolt, A. U. 1992, AJ, 104, 340

Lo, K. Y., Sargent, W. L. W., & Young, K. 1993, AJ, 106, 507

Martin, C. 1998, ApJ, 506, 222

Martin, P. 1995, AJ, 109, 2428

Meurer, G. R., Carignan, C., Beaulieu, S. F., & Freeman, K. C. 1996, AJ, 111, 1551

Meurer, G. R., Staveley-Smith, L, & Killeen, N. E. B. 1998, MNRAS, 300, 705

Noeske, K. G., Guseva, N. G., Fricke, K. J., Izotov, Y. I., Papaderos, P., & Thuan, T. X. 2000, A&A, 361, 33

Ohta, K., Hamabe, M., & Wakamatsu, K. 1990, ApJ, 357, 71

Ondrechen, M. P., & van der Hulst, J. M. 1989, ApJ, 342, 29

Pierini, D., Gavazzi, G., Boselli, A., & Tuffs, R. 1997, A&AS, 125, 293

Pisano, D. J., Wilcots, E. M., & Elmegreen, B. G. 1998, AJ, 115, 975

Puche, D., Westpfahl, D., Brinks, E., Roy, J.-R. 1992, AJ, 103, 1841

Quirk, W. J. 1972, ApJ, 176, L9

Richter, O.-G., & Sancisi, R. 1994, A&A, 290, L9

Roberts, M. S. 1969, AJ, 74, 859

Roberts, M. S., & Haynes, M. P. 1994, ARA&A, 32, 115

Roy, J.-R., Aubé, M., McCall, M. L., & Dufour, R. J. 1992, ApJ, 386, 498

Roy, J.-R., Boulesteix, J., Joncas, G., & Grundseth, B. 1991, ApJ, 367, 141

Roye, E. W., & Hunter, D. A. 2000, AJ, 119, 1145

Rubio, M., Garay, G., Montanai, J., & Thaddeus, P. 1991, ApJ, 368, 173

Safronov, V. S. 1960, Ann.d'Ap., 23, 979

Salpeter, E. E. 1955, ApJ, 121, 161

Sargent, W. L. W., Sancisi, R., & Lo, K. Y. 1983, ApJ, 265, 711

Simpson, C. E. 1995, PhD Thesis, U Florida

Skillman, E. D. 1987, in Star Formation in Galaxies, ed. C. Persson (Washington:GPO), p 263

Skillman, E. D., Terlevich, R., Teuben, P. J., & van Woerden, H. 1988, A&A, 198, 33

Swaters, R. 1999, PhD Thesis, Rijksuniversiteit Groningen

Taylor, C. L., Brinks, E., Pogge, R. W., & Skillman, E. D. 1994, AJ, 107, 971

Thornley, M. D., & Wilson, C. D. 1995, ApJ, 447, 616

Thuan, T. X., & Martin, G. E. 1981, ApJ, 247, 823

Tolstoy, E., Saha, A., Hoessel, J. G., & McQuade, K. 1995, AJ, 110, 1640

Toomre, A. 1964, ApJ, 139, 1217

Tully, R. B., Bottinelli, L., Fisher, J. R., Gouguenheim, L., Sancisi, R., & van Woerden, H. 1978, A&A, 63, 37

van den Bergh, S. 1988, PASP, 100, 344

van der Hulst, J. M., Skillman, E. D., Smith, T. R., Bothun, G. D., McGaugh, S. S., & de Blok, W. J. G. 1993, AJ, 106, 548

van Zee, L., Haynes, M. P., Salzer, J. J., & Broeils, A. H. 1997, AJ, 113, 1618

van Zee, L, Skillman, E. D., & Salzer, J. J. 1998, AJ, 116, 1186

Wada, K., Spaans, M., Kim, S. 2000, ApJ, 540, 797

Warmels, R. H. 1988, A&AS, 73, 453

Wevers, B. M. H. R. 1984, Ph.D. Thesis, Rijksuniversiteit Groningen

Wevers, B. M. H. R., van der Kruit, P. C., & Allen, R. J. 1986, A&AS, 66, 505

Wilcots, E. M., & Miller, B. W. 1998, ApJ, 116, 2363

Wilcots, E. M., & Thurow, J. C. 2001, ApJ, in press

Yang, H., Skillman, E. D., & Sramek, R. A. 1994, AJ, 107, 651

Young, L. M., & Lo, K. Y. 1996, ApJ, 462, 203

Young, L. M., & Lo, K. Y. 1997, ApJ, 490, 710

Youngblood, A. J., & Hunter, D. A. 1999, ApJ, 519, 55

This preprint was prepared with the AAS IATEX macros v4.0.

- Fig. 1.— Integrated velocity profile made by summing flux over square boxes 10′ and 30′ on a side. The larger box is approximately the primary beam size of the VLA telescope. The fluxes are corrected for the attenuation by the primary beam. This is compared to the profiles obtained with a single-dish radio telescope with a 10′ beam by Hunter, Gallagher, & Rautenkranz (1982).
- Fig. 2.— 21-cm continuum map shows the continuum sources within the primary beam of the VLA data. The map has been corrected for the attenuation by the primary beam. The continuum sources are numbered as given in Table 1. The beam size FWHM $(33.6'' \times 28.9'')$ is shown as the tiny elliptical contour in the lower left corner near 7^h 26^m 20^s , 69° , 01'.
- Fig. 3.— $H\alpha$ image of NGC 2366 shown superposed with contours from the 21 cm continuum map. Contours are 1 to 7 mJy beam⁻¹ in steps of 1 mJy beam⁻¹. The contour in the lower left corner represents the FWHM of the synthesized beam $(33.6'' \times 28.9'')$.
- Fig. 4.— V-band image of NGC 2366. Contours are of the V-band image smoothed 14×14 pixels. The inner contour is of a surface brightness level of 25.66 magnitudes $\operatorname{arcsec}^{-2}$, and the outer is 26.54 magnitudes $\operatorname{arcsec}^{-2}$. The inner contour highlights the region fit as a bar, and the smooth ellipse is a bar structure with c=3.0 and a semi-major axis of 4.3′. The outer contour highlights the region of low surface brightness that extends the major axis to the southwest. For orientation, one can use the upper of two tiny elliptical contours within the body of the galaxy to note the approximate location of NGC 2363. Residuals of a saturated star are visible along the top edge of the image.
- Fig. 5.— V-band image of NGC 2366. Contours are of the V-band image smoothed 14×14 pixels, at surface brightness levels of 25.66, 24.04, 23.04, and 22.68 magnitudes arcsec⁻². The smooth ellipses are the fits to bar structures discussed in the text with c = 3.0.
- Fig. 6.— Surface brightness cuts along the inner bar in the V-band image of NGC 2366 (Figure 5). Cuts along the major axis (position angle 32.5°) and along the minor axis are shown. Both were constructed by summing over 33". The spike in the major-axis profile is due to the supergiant H II complex NGC 2363. The left side of the graph refers to the southeast side of the minor axis and the northeast side of the major axis. The vertical dashed lines mark the semi-major axis of the inner bar.
- Fig. 7.— UBV surface photometry of NGC 2366. The photometry is corrected for an internal reddening of 0.05 mag and an external reddening of 0.043 mag. The exponential fit to the V-band surface brightness profile is shown as a solid line. The spike at 1.2′ is due to the supergiant H II complex NGC 2363.
- Fig. 8.— JHK surface photometry of NGC 2366. The fit to the V-band surface brightness profile is shown for comparison; it has been shifted vertically to match the J-band brightness. The spike at 1' is due to the supergiant H II complex NGC 2363.

- Fig. 9.— False-color display of the optical B/V ratio image, averaged 3×3 pixels to improve signal-to-noise. Blue color in the display denotes a higher B/V (bluer) ratio in the galaxy. The exceptions are regions of bright foreground stars that produce the large red circular region at $\sim 7^h$ 23^m 30^s , 69° 21' and the mess along the upper edge to right of middle of the display. Contours are from the V-band image smoothed 14×14 pixels and are 26.54, 25.66, 24.04, 23.04, and 22.68 magnitudes arcsec⁻²; these are the same contours as shown in Figures 4 and 5.
- Fig. 10.— Azimuthally-averaged H α surface brightness and reddening-corrected V-band surface brightness. The H α luminosity is proportional to the star formation rate and was corrected for extinction using an A_{H α} of 0.36 magnitude. The scales for $\Sigma_{H\alpha,0}$ and μ_V^0 have been set so that they cover the same logarithmic interval. The spike at 1.2' is due to the supergiant H II complex NGC 2363.
- Fig. 11.— Channel maps of HI line-emission in NGC 2366 made from observations with the VLA C and D-arrays, centered on the optical galaxy. The inner $19' \times 19'$ are shown. The beam size FWHM $(33.6'' \times 28.9'')$ is shown in the final panel of the channel maps.
- Fig. 12.— Integrated HI map of NGC 2366. Shallow display (left) shows the central HI ring; deep display (right) shows structure in the outer HI. The contour is of the V-band image of the galaxy smoothed 14×14 and at a surface brightness level of 25.66 magnitudes $\operatorname{arcsec}^{-2}$. The FWHM of the synthesized beam, shown as the ellipse in the lower left corner of each panel, is $33.6''\times28.9''$.
- Fig. 13.— Surface density of HI for NGC 2366 is computed in two ways: closed circles—using the position angle (23°) and inclination (73°) of the HI morphology; open circles—using the position angle (46°) and inclination (65°) of the HI kinematics. Left: For comparison we show the average HI surface density profile of a sample of Im, Sdm, and Sd galaxies. Those data are from Cayatte et al. (1994) and Broeils & van Woerden (1994). These references normalize the radius to R_o , a radius given by de Vaucouleurs et al. (1991). In most cases R_o is nearly the same as R_{25} , the normalization we use for NGC 2366. The x-axis at the top of the figure is R in arcminutes for NGC 2366 only. Right: In order to compare the HI surface density with that of $H\alpha$ and the starlight, we show the logarithm of Σ_{HI} . The V-band and $H\alpha$ surface brightness profiles of NGC 2366 are also shown. The scale for the $H\alpha$ surface brightness, not shown, goes from a logarithm of 30.75 to 34.25 with units of ergs s⁻¹ pc⁻². The plotting scales are chosen so that a magnitude interval corresponds to 0.4 of the invertal for logarithmic quantities and all logarithmic quantities are plotted over the same number of dex.
- Fig. 14.— HI column density contours superposed on our H α image. The HI contours are 0.88, 3.8, 6.8, 9.7, 15.6, 21.5, 27.4, 33.3, 39.2, and 45.0 $\times 10^{20}$ atoms cm⁻². The ellipse in the lower left corner is the FWHM of the synthesized beam (33.6" \times 28.9").
- Fig. 15.— Brightnesses of individual pixels are compared in HI and H α . The H α image was averaged 15×15 to produce a pixel scale of 6.3", close to the pixel scale of the HI map. The x-axis is the HI pixel brightness in mJy beam⁻¹ where 1 mJy beam⁻¹ corresponds to a column density of

 5.9×10^{18} atoms cm⁻². The y-axis is the logarithm of the H α pixel brightness in counts in the image where 1 count corresponds to an H α luminosity of 1.15×10^{33} ergs s⁻¹, corrected for reddening.

Fig. 16.— Color-coded display of the HI velocity field. The beam size (FWHM shown in the lower left corner) is $33.6'' \times 28.9''$ and the velocity resolution is 10 km s^{-1} . In the upper panel the contours are of the model best-fit velocity field at 60, 80, 100, 120, and 140 km s⁻¹. In the bottom panel, the outer contour is the inner V-band contour shown in Figure 4; and the inner contour is of the $H\alpha$ image. The units of the color wedge are km s⁻¹.

Fig. 17.— Top panel: Best-fit rotation curve. The rotation curve comes from fitting rings of 20" width out to a radius of 460" and 40" width beyond that to a radius of 620". The center position, systemic velocity (99 km s⁻¹), position angle (46°), and inclination (65°) were fixed in the final fit. The kinematics of the approaching side of the galaxy are peculiar and not well fit by the model. The horizontal dashed line at 40 km s⁻¹ is an aid to the eye in following the rotation curve. Middle panel: Position angle for tilted ring model fits to the velocity field. A position angle was determined from the central part of the velocity field with emphasis on the well-behaved receding part of the galaxy. The dashed horizontal line marks the value of the final position angle. Bottom panel: Inclination for tilted ring model fits to the velocity field. An inclination was determined from the central part of the velocity field with emphasis on the well-behaved receding part of the galaxy. The dashed horizontal line marks the value of the final inclination angle.

Fig. 18.— Color-coded display of the HI velocity dispersion. The small ellipse in the lower, left corner is the FWHM of the beam $(33.6'' \times 28.9'')$. In the top panel the outer contour is the outer V-band contour shown in Figure 4. The inner contour is of the H α image and corresponds to 1.7×10^{34} ergs s⁻¹ arcsec⁻². In the middle panel the contours are of the velocity field map and correspond to 60 km s⁻¹ to 140 km s⁻¹ in steps of 10 km s⁻¹. In the bottom panel the contours outline the integrated HI map and are 3.5, 7.1, 10.6, 14.1, 21.5, 33.3, and 45.0×10^{20} atoms cm⁻². The units of the color wedge are km s⁻¹.

Fig. 19.— HI line profiles for the region of high HI velocity dispersion on the eastern edge of the HI distribution. Every five pixels, approximately one beam-width, have been averaged. Flat-top profiles are profiles whose tops have been chopped off in plotting in order to be able to show the weaker profiles.

Fig. 20.— East—west scans of HI column densities (dashed lines) and velocity dispersions (solid lines) across the disk of NGC 2366, averaged over one beam width in declination. Each goes through a region where the velocity dispersion has a sudden increase in the outer part of the disk. In the main part of the galaxy, the velocity dispersion anticorrelates with the column density, suggesting that turbulent motions are faster in the lower density regions.

Fig. 21.— Region of the supergiant H II complex NGC 2363. The gray-scale is $H\alpha$, and the contours are the integrated C-array HI. The contours are 2.43×10^{21} atoms cm⁻² to 6.68×10^{21} atoms cm⁻², in steps of 6.075×10^{20} atoms cm⁻². The ellipse in the lower left corner is the FWHM of the HI

beam, $17.8'' \times 13.2''$ (300 pc×220 pc at the galaxy).

Fig. 22.— Region of the galaxy including the supergiant H II complex NGC 2363. The gray-scale is H α , and the contours are the C-array HI velocity field. The contours begin with 60 km s⁻¹ at the far right and go to 105 km s⁻¹ in the upper left corner in steps of 5 km s⁻¹. The ellipse in the lower right corner is the FWHM of the HI beam, $17.8'' \times 13.2''$ (300 pc×220 pc at the galaxy).

Fig. 23.— HI line profiles from the C-array data for a region centered on NGC 2363. The data cube has been averaged over five pixels (15"), approximately one beam-width.

Fig. 24.— Surface densities in NGC 2366. The dashed vertical lines mark radii where the rotation curve (Figure 17) ceases to be that of a solid body (left) and where it begins to turn over (right). The critical gas density for the thin-rotating disk model Σ_c is determined from the rotation curve of the galaxy and the mean velocity dispersion, determined as a function of radius from the C+D-array second moment map. The azimuthally-averaged gas surface density Σ_g is determined assuming a position angle of 46 ° and an inclination of 65° and is corrected for the presence of He and, statistically, for H₂. The Σ_g (max) are the maximum surface densities of the gas in the vicinity of each H II region in the galaxy. The $\Sigma_{H\alpha}$ are the H α surface brightnesses measured from the H α image using the optically-derived position angle of 32.5° and 72°. $\Sigma_{H\alpha}$ shows where star formation is taking place within the galaxy. The Σ_T are limiting tidal densities.

This figure "f1.gif" is available in "gif" format from:

This figure "f11_1.gif" is available in "gif" format from:

This figure "f11_2.gif" is available in "gif" format from:

This figure "f2.gif" is available in "gif" format from:

This figure "f3.gif" is available in "gif" format from:

This figure "f4.gif" is available in "gif" format from:

This figure "f5.gif" is available in "gif" format from:



This figure "f7.gif" is available in "gif" format from:

This figure "f8.gif" is available in "gif" format from:

This figure "f9.gif" is available in "gif" format from:

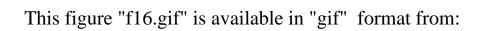
This figure "f10.gif" is available in "gif" format from:

This figure "f12.gif" is available in "gif" format from:

This figure "f13.gif" is available in "gif" format from:

This figure "f14.gif" is available in "gif" format from:

This figure "f15.gif" is available in "gif" format from:



This figure "f17.gif" is available in "gif" format from:

This figure "f18.gif" is available in "gif" format from:

This figure "f19.gif" is available in "gif" format from:

This figure "f20.gif" is available in "gif" format from:

This figure "f21.gif" is available in "gif" format from:

This figure "f22.gif" is available in "gif" format from:

This figure "f23.gif" is available in "gif" format from:

This figure "f24.gif" is available in "gif" format from: